A national laboratory of the U.S. Department of Energy
Office of Energy Efficiency & Renewable Energy

NREL National Renewable Energy Laboratory
Innovation for Our Energy Future

Identifying Electronic Properties Relevant to Improving the Performance and Stability of Amorphous Silicon Based Photovoltaic Cells

Final Subcontract Report
27 November 2002–31 March 2005

Subcontract Report
NREL/SR-520-38676
November 2005

J.D. Cohen
University of Oregon
Eugene, Oregon

NREL is operated by Midwest Research Institute • Battelle   Contract No. DE-AC36-99-GO10337

Identifying Electronic Properties Relevant to Improving the Performance and Stability of Amorphous Silicon Based Photovoltaic Cells

Subcontract Report
NREL/SR-520-38676
November 2005

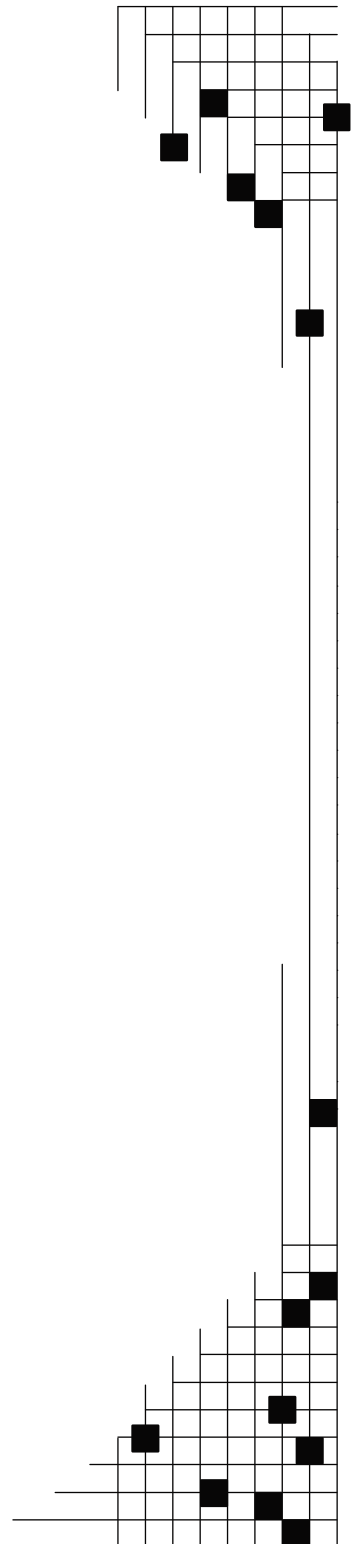

Final Subcontract Report
27 November 2002–31 March 2005

J.D. Cohen
University of Oregon
Eugene, Oregon

NREL Technical Monitor: Bolko von Roedern
Prepared under Subcontract No. ADJ-2-30630-17

National Renewable Energy Laboratory
1617 Cole Boulevard, Golden, Colorado 80401-3393
303-275-3000 • www.nrel.gov

Operated for the U.S. Department of Energy
Office of Energy Efficiency and Renewable Energy
by Midwest Research Institute • Battelle

Contract No. DE-AC36-99-GO10337

This publication was reproduced from the best available copy submitted by the subcontractor and received no editorial review at NREL.

NOTICE

This report was prepared as an account of work sponsored by an agency of the United States government. Neither the United States government nor any agency thereof, nor any of their employees, makes any warranty, express or implied, or assumes any legal liability or responsibility for the accuracy, completeness, or usefulness of any information, apparatus, product, or process disclosed, or represents that its use would not infringe privately owned rights. Reference herein to any specific commercial product, process, or service by trade name, trademark, manufacturer, or otherwise does not necessarily constitute or imply its endorsement, recommendation, or favoring by the United States government or any agency thereof. The views and opinions of authors expressed herein do not necessarily state or reflect those of the United States government or any agency thereof.

Available electronically at http://www.osti.gov/bridge

Available for a processing fee to U.S. Department of Energy and its contractors, in paper, from:
U.S. Department of Energy
Office of Scientific and Technical Information
P.O. Box 62
Oak Ridge, TN 37831-0062
phone: 865.576.8401
fax: 865.576.5728
email: mailto:reports@adonis.osti.gov

Available for sale to the public, in paper, from:
U.S. Department of Commerce
National Technical Information Service
5285 Port Royal Road
Springfield, VA 22161
phone: 800.553.6847
fax: 703.605.6900
email: orders@ntis.fedworld.gov
online ordering: http://www.ntis.gov/ordering.htm

Printed on paper containing at least 50% wastepaper, including 20% postconsumer waste

PREFACE

This Annual Technical Progress Report covers the work performed at the University of Oregon for the period 27 November 2002- 31 March 2005 under NREL Subcontract Number ADJ-2-30630-17. The following personnel participated in this research program:

NAME	TITLE	WORK PERFORMED
J. David Cohen	Principal Investigator	Program Manager
Shouvik Datta	Research Associate	Properties of NREL HWCVD a-Si,Ge:H alloys
Jennifer Heath	Research Assistant	Properties of BP Solar a-Si:H samples deposited at high rates.
Suman Iyer	Visiting Scientist	Properties of BP Solar a-Si:H samples deposited at high rates.
James Gutierrez	Research Assistant	Properties of Iowa State a- Ge:H samples and United Solar nanocrystalline Si materials
Adam Halverson	Research Assistant	Properties of United Solar nanocrystalline Si material

TABLE OF CONTENTS

Page

LIST OF ILLUSTRATIONS vi

LIST OF TABLES viii

EXECUTIVE SUMMARY ix

1.0 INTRODUCTION 1

2.0 SAMPLES 2

- 2.1 UNITED SOLAR NANOCRYSTALLINE SILICON 2
- 2.2 UNITED SOLAR AMORPHOUS SILICON NEAR MICROCRYSTALLINITY 2
- 2.3 BP SOLAR HIGH GROWTH RATE AMORPHOUS SILICON SAMPLES 3
- 2.4 NREL HOT-WIRE CVD AMORPHOUS SILICON-GERMANIUM ALLOYS 4
- 2.5 IOWA STATE AMORPHOUS GERMANIUM 5

3.0 EXPERIMENTAL CHARACTERIZATION METHODS 6

- 3.1 ADMITTANCE SPECTROSCOPY 6
- 3.2 DRIVE-LEVEL CAPACITANCE PROFILING 7
- 3.3 TRANSIENT PHOTOCAPACITANCE AND PHOTOCURRENT 7

4.0 PROPERTIES OF UNITED SOLAR NANOCRYSTALLINE SILICON 10

- 4.1 ADMITTANCE AND DRIVE-LEVEL CAPACITANCE PROFILING STUDIES 10
- 4.2 SUB-BAND-GAP PHOTOCAPACITANCE SPECTROSCOPY 13
- 4.3 LIGHT INDUCED EFFECTS IN NANOCRYSTALLINE SILICON 17

5.0 UNITED SOLAR AMORPHOUS SILICON NEAR PHASE BOUNDARY 19

6.0 BP SOLAR HIGH GROWTH RATE AMORPHOUS SILICON SAMPLES 21

- 6.1 REVIEW OF PREVIOUSLY REPORTED RESULTS 21
- 6.2 CORRELATION BETWEEN DEFECT DENSITIES AND DEVICE PERFORMANCE 23
- 6.3 STUDIES ON NEW SERIES OF BP SOLAR HIGH GROWTH RATE SAMPLES 25

7.0 NREL HOT-WIRE AMORPHOUS SILICON-GERMANIUM ALLOYS 31

- 7.1 GENERAL ELECTRONIC PROPERTIES 31
- 7.2 LIGHT-INDUCED DEGRADATION IN HWCVD a-Si,Ge:H 34

8.0 ELECTRONIC PROPERTIES OF ECR DEPOSITED AMORPHOUS GERMANIUM 36

9.0 SUMMARY AND CONCLUSIONS 37

10.0 SUBCONTRACT SUPPORTED PUBLICATIONS 40

11.0 REFERENCES 41

LIST OF ILLUSTRATIONS

Page

FIG. 1 Schematic of the appearance of United Solar samples deposited very close to the amorphous/microcrystalline phase boundary 3

FIG. 2(a) Capacitance and conductance vs. temperature for Iowa State a-Ge:H
2(b) Arrhenius plot of the inflection points of the capacitance step vs. frequency 6

FIG. 3. Schematic of four different types of sub-bandgap optical transitions 8

FIG. 4 Variation of the junction capacitance with voltage for the 14140 a-Si:H/nc-Si:H/a-Si:H sandwich sample 10

FIG. 5(a) Capacitance vs. temperature for one multilayer sample at 7 measurement frequencies
5(b) Arrhenius plot of large capacitance step reveals an activation energy near 0.5eV... 11

FIG. 6. DLCP curves for the pin nc-Si:H device sample 12123 12

FIG. 7. DLCP curves for the a-Si:H/nc-Si:H/a-Si:H multilayer sample 14140 12

FIG. 8. DLCP curves for nc-Si:H deposited under conditions of hydrogen profiling 13

FIG. 9. CPM spectrum for μc-Si:H taken from the paper by M. Vaneček et al 14

FIG. 10. TPC spectra for one sandwich nc-Si:H sample device at three measurement temperatures 14

FIG. 11(a) Photocapacitance spectra for one a-Si:H/nc-Si:H/a-Si:H multilayer sample at two measurement temperatures
(b) Transient junction photocurrent spectra for the same temperatures 15

FIG. 12. Photocapacitance spectra for the pin nc-Si:H device at two similar temperatures 15

FIG. 13. Temperature dependence of the TPC signal near a 1.5eV optical energy 16

FIG. 14. Drive-level capacitance profiles taken at various stages of light soaking 17

FIG. 15. Comparison of TPC spectra in State A at 180K and 240K, along with the TPC spectrum at 240K after prolonged light exposure 18

FIG. 16. Detailed temperature dependence in State A and State B of the TPC signal magnitude near 1.5 eV 18

FIG. 17. TPC spectra at two measurement temperatures for a series of metastable states produced by partial annealing a fully light soaked state 19

FIG. 18(a) DLC profiles for region near center of United Solar film L13698 in State A
18(b) DLC profiles for same region of film after degradation 20

FIG. 19(a) A monotonic loss of device efficiency in the degraded state is observed with increasing growth rate
19(b) Defect densities obtained from DLCP measurements are roughly independent of growth rate for both state A and the light-degraded state B 21

FIG. 20(a) Photocapacitance spectra for a 1.5Å/s growth rate sample in both the annealed state and the light-degraded state.
20(b) Example of how spectra are fit with an exponential bandtail plus a Gaussian shaped defect band.. 22

FIG. 21 The Urbach energies deduced from the photocapacitance spectra correlate fairly strongly with the sample growth rates... 23

FIG. 22(a) Magnitude of deep defect band deduced from TPC spectra vs. matched device fill factor
22(b) Defect band magnitudes determined from TPC spectra in states A and B are related by nearly a constant factor 24

FIG. 23 Drive-level capacitance profiles for BP Solar sample L2129 (3Å/s) in the dark annealed state 27

FIG. 24 Deep defect densities vs. growth rate for BP Solar films for both States A and B... 27

FIG. 25(a) Photocapacitance spectra for BP Solar sample L2127 (1Å/s) taken at 380K at two values of reverse bias
25(b) CPM spectra obtained at NREL for the same sample.. 28

FIG. 26 Urbach energies determined from TPC spectra vs. film growth rate........................ 29

FIG. 27 Photocapacitance spectra for two BP Solar films (deposited at 1Å/s and 10Å/s) in State A.. 30

FIG. 28 Previous TPC spectra of NREL HWCVD alloy material 32

FIG. 29 TPC spectra of the low filament temperature HWCVD samples with 15 , 29, and 47at.% Ge 32

FIG. 30 Drive-level capacitance profiling reveals very low midgap defect densities for the a-Si,Ge:H samples with Ge fractions of 15, 29, and 47at.% 33

FIG. 31 Comparison of TPC and TPI spectra for the 29at.% Ge sample.............................. 34

FIG. 32(a) Spatial profile of mid gap densities after increasing periods of light exposure for the 29at.% Ge sample
32(b) Time dependence of the average midgap density with increasing light soaking.... 35

FIG. 33 Comparsion of the mid band-gap defect band for three photocapacitance spectra of the 29at.% Ge sample 35

FIG. 34 Drive-level capacitance profiles of Iowa State ECR deposited a-Ge:H 36

FIG. 35 Transient photocapacitance and transient junction photocurrent spectra for Iowa State a-Ge:H sample 37

LIST OF TABLES

TABLE I. United Solar nc-Si:H samples studied during this Subcontract period. 2

TABLE II. Characteristics of HWCVD a-Si,Ge:H films obtained from NREL 5

TABLE III. BP Solar film results for samples in the annealed state (State A) and after light soaking (State B) are listed in order of increasing growth rate 24

TABLE IV. Summary of cell parameters in State A for matched BP Solar devices 26

TABLE V. Comparison of TPC determined Urbach energies of BP Solar samples with growth rate, as well as hydrogen content (NREL), void fraction (CSM), and CPM determined Urbach energies (NREL) 29

TABLE VI. Summary NREL low filament temperature HWCVD a-Si,Ge:H sample electronic properties.. 32

EXECUTIVE SUMMARY

Our work under NREL Subcontract ADJ-2-30630-17 has focused on three areas of study. First, we used DLCP and transient photocapacitance (TPC) spectroscopy to characterize the electronic properties of hydrogenated nanocrystalline Si (nc-Si:H) produced at United Solar Ovonics Corporation. We found DLCP state densities in the 10^{15} to 10^{16} cm^{-3} range and found for the three samples deposited under constant hydrogen dilution that these increased in the direction of film growth. This is consistent with observations at USOC that the crystallite size increases as the films become thicker, and this also leads to an increase in deep defect density. However, one sample deposited using hydrogen profiling showed a very different spatial distribution of these defects, as well as lower densities overall. Our transient photocapacitance measurements disclosed a sub-band-gap spectrum that evolved from a very μc-Si:H appearance at lower temperatures (200K), to a very a-Si:H like in appearance at moderate temperatures (300K). By comparing TPC with transient photocurrent (TPI) spectra we demonstrated that this change in appearance results from improving hole carrier collection as the temperature is increased which then diminishes the photocapacitance response of the nanocrystalline component in these materials relative to the a-Si:H component in these mixed phase samples. By examining the temperature dependence of the TPC spectra in detail, we determined that the hole collection was thermally activated, with an activation energy near 0.2eV. This suggests a dominant hole trap that impedes the minority carrier collection from the nanocrystallite phase of these samples.

We also examined the effects of light-induced degradation in some detail for one of the nc-Si:H samples. The DLCP measurements actually showed very little change with light soaking, even after 100 hours at $100 mW/cm^2$. However, significant degradation in the hole carrier collection were observed in the TPC measurements, by nearly a factor of 50 at most temperatures. However, we did not observe any increase in any spectral feature, including the dangling bond defect band, that might be responsible for the observed loss in hole collection.

A second focus was continued work to try to identify the fundamental reasons that higher growth rate a-Si:H materials lead to devices with generally lower performance. These studies utilized series of samples produced by Gautam Ganguly at BP Solar. Previously, our measurements had revealed that the deep defect density determined by drive-level capacitance profiling (DLCP) did not change as the growth rate was varied; however, the Urbach energies deduced by transient photocapacitance (TPC) sub-band-gap spectroscopy *were* correlated with growth rate and hence also the device performance. During the current Subcontract we found that the magnitudes of the deep defect revealed in the TPC spectra also correlated quite well with the device fill factors, even though the DLCP determined defect densities did not. Thus we now suggest that the capture cross section of the deep defects are enhanced at the higher growth rates even though their actual density do not vary substantially.

We also report results on a new series of samples deposited by Gautam Ganguly at BP Solar. Here our own work was one part of a five-way collaboration with NREL, Colorado School of Mines, University of North Carolina, and BP Solar. Results for this new series of samples agreed with the previous set in that the DLCP determined defect densities appeared to be largely uncorrelated with device performance, while the Urbach energies were strongly correlated. The other studies of the collaboration revealed that the void fraction and the hydrogen content were also quite strongly correlated with growth rate. Once again, the cell performance exhibited a systematic decline in performance with increasing growth rate.

The third area of focus was to evaluate a new class of hot-wire deposited a-Si,Ge:H alloy samples produced at NREL that were deposited using a Ta filament operated at 1800°C instead of a tungsten filament at 2000°C that had been used in the past. Previously, for the HWCVD a-Si,Ge:H alloys deposited using the higher filament temperature, even modest Ge fractions were found to result in Urbach energies in excess of 55meV and also to correspondingly large defect densities. In contrast we found dramatically improved properties for the new class of alloy materials. Photocapacitance and DLCP measurements on three of these HWCVD a-Si,Ge:H alloys with Ge fractions of 15, 29, and 47at.% were found to exhibit narrow band tails (of 45meV or less) and midgap defect densities as low as the best PECVD grown alloy samples. These results thus directly corroborate the SAXS data indicating very uniform film structure with fewer micro-structural defects compared to previous a-Si,Ge:H alloys.

On the other hand, when we compared the photocapacitance spectra with the corresponding transient photocurrent spectra, this indicated that minority hole collection was less efficient than the best PECVD grown alloy materials. This is puzzling given the very narrow bandtails, and further measurements are planned to better understand this result. Some preliminary light induced degradation studies on one (29at.% Ge) sample were also carried out. These revealed a roughly a 4-fold increase in mid-gap defect densities but also a novel two step defect creation process.

In addition to these three major focus areas, we examined a couple of amorphous germanium (a-Ge:H) samples produced by the ECR method at Iowa State University. Our studies of the ECR a-Ge:H indicated quite superior electronic properties of the Iowa State a-Ge:H material, both in terms of the DLCP deduced defect densities, and the TPC deduced Urbach energies. Also, we characterized several United Solar a-Si:H samples deposited very close to the microcrystalline phase transition. These exhibited quite good electronic properties with midgap defect densities slightly less than 1×10^{16} cm^{-3} in the fully light-degraded state.

1.0 INTRODUCTION

The work carried out under NREL Subcontract ADJ-2-30630-17 has focused primarily on three subject areas. A major effort during this subcontract period has been to evaluate the microcrystalline Si material under development at United Solar Ovonics Corporation (USOC). This material is actually a hydrogenated nanocrystalline form of Si and it will be denoted in this report as nc-Si:H. It is hoped that such materials may ultimately be able to replace one of a-Si,Ge:H layers in an amorphous silicon triple junction device. Our junction capacitance methods have revealed a substantial amorphous silicon component to these nc-Si:H materials and provide sub-band-gap spectra of both the nanocrystallite and amorphous silicon phases. Moreover, we have been able to deduce that under light induced degradation the minority carrier collection fraction is substantially reduced. This may account for the light-induced degradation that is observed in many nc-Si:H based devices.

In our second focus area, we continued our studies of the BP Solar high growth samples that we began under our previous NREL Subcontract (XAF-8-17619-05). Previously we had found that, although the cell performance showed a strong negative correlation with deposition rate, the deep defect densities in either the annealed or degraded states did not exhibit any marked change with growth rate. However, we had found a strong correlation between Urbach energy and growth rate. During the first year of the just completed Subcontract we discovered that the magnitudes of the deep defect band revealed in our sub-band-gap photocapacitance spectra *did correlate* inversely with the device performance even though the DLCP density did not. We propose a possible explanation for this. Following this, we took part in a five-way collaborative study examining a new series of BP Solar samples of varying growth rate. The results on this new series of samples were found to be consistent with those on the previous set of samples.

Our third major focus has been in the evaluation of amorphous silicon-germanium alloys produced by the hot-wire CVD growth process at NREL. This method holds some potential for higher deposition rate Ge alloy materials with good electronic properties. Previous HWCVD a-Si,Ge:H were always found to have inferior electronic properties to material produced by PECVD; however, the new series of samples, deposited using lower filament temperatures have revealed superior electronic properties in the first set of results we have obtained.

In addition to these three major focus areas, we also examined some a-Ge:H samples prepared using the ECR growth technique in Vikram Dalal's laboratory at Iowa State University. These appear to have notably very good electronic properties. We also characterized a few more United Solar a-Si:H samples deposited very close to the microcrystalline phase transition.

2.0 SAMPLES

2.1 UNITED SOLAR NANOCRYSTALLINE SILICON

All of the nc-Si:H sample devices were deposited onto specular stainless steel (SS) substrates at United Solar using an rf PECVD process. They are listed in Table I. Three "sandwich" devices consisted of roughly 700-nm thick nc-Si:H layers clad between two 200 to 250-nm thick a-Si:H layers in a SS/n+/a-Si:H/nc-Si:H/a-Si:H structure. We deposited a Pd Schottky barrier on top of each to finish these sandwich sample devices for our measurements. For one of these samples (14140) the nc-Si:H was deposited using constant hydrogen dilution, a second (14657) employed 25% less hydrogen, while for the third (14661) the hydrogen dilution was varied to control the evolution of crystalline volume fraction and crystallite size [1]. In addition we examined one purely nc-Si:H p-i-n device (12123) containing a 1000-nm thick intrinsic layer that had a SS/n^+/i/p^+/ITO structure. This was deposited using a constant level of hydrogen dilution.

There are a couple of reasons for fabricating and characterizing nc-Si:H in both sandwich and p-i-n devices. First, we wanted to discriminate against effects of possible oxygen contamination of the nc-Si:H which are inhibited by the a-Si:H cladding layers in the sandwich structure. We expect these a-Si:H layers to behave only as insulating layers in our measurements because we work at sufficiently low temperatures. Results on the p-i-n structure can be used to check this since it only contains nc-Si:H. However, the p-i-n sample also contains heavily doped n and p layers, which may also partially mask the response due to the intrinsic layer itself.

2.2 UNITED SOLAR AMORPHOUS SILICON NEAR MICROCRYSTALLINITY

During this Subcontract period we also attempted to examine the metastable properties of a-Si:H films deposited near and just beyond the edge of the microcrystalline phase transition. We obtained two sample arrays from United Solar, each of which was produced in a single

Table I. United Solar nc-Si:H samples studied during the Subcontract period.

Sample #	Device Type	nc-Si:H thickness (nm)	Hydrogen Dilution	a-Si:H layer thickness (nm)
14140	Sandwich	770	Standard	2x250
14657	Sandwich	640	25% Less	2x250
14661	Sandwich	700	Profiled	2x250
12123	p-i-n	1000	Standard	None

FIG. 1. Schematic of the appearance of United Solar samples L13690 and L13698. These films were deposited very close to the amorphous/microcrystalline phase boundary. The innermost circle was the most amorphous in appearance, the next 2 concentric circles appeared much grayer due to their increasing microcrystalline fraction. We deposited Pd 1mm diameter dots across one quardrant of each sample as indicated to attempt to explore the variation in electronic properties as the microcrystalline fraction was increased.

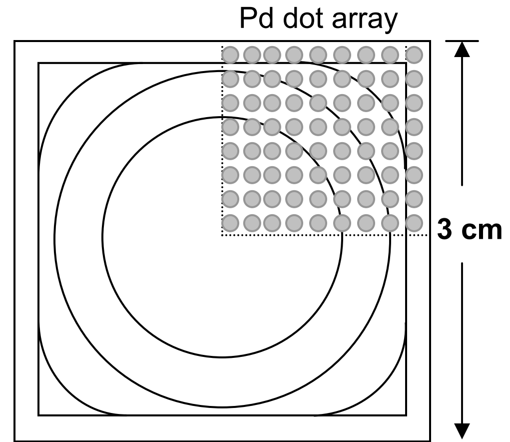

deposition, but which ranged from nearly purely amorphous to very microcrystalline over a 1-2 cm distance. Such samples can be produced in their glow discharge reaction using a level of hydrogen dilution very close to the value of the amorphous to microcrystalline phase boundary. This meant that the small rf power density variation across the diameter of the 2” x 2” substrate resulted in variations of the microcrystalline fraction in a very significant manner. The sample structures were SS/n/i with the i layers roughly 2 microns thick. A schematic diagram of the different regions the occur in the two samples we received in shown in Fig. 1 above.

These films are similar to the array of cells researchers at United Solar employed in their recently reported study in which an unusual variation in open circuit voltage with light-induced degradation was observed depending on the microcrystalline fraction in that part of the sample.[2] Thus, we hoped to gain some insight into the changes in the electronic properties of these films (in going from more amorphous to more microcrystalline) to understand the unusual changes in V_{OC} with light soaking that were disclosed in the United Solar study.

2.3 BP SOLAR HIGH GROWTH RATE AMORPHOUS SILICON SAMPLES

Under our previous NREL Subcontract Gautam Ganguly at BP Solar had sent us a series of of nine samples to examine the properties of these DC glow discharge a-Si:H films as the growth rate varied due to different levels of hydrogen dilution and glow discharge power. For this set of samples the growth rate varied between 0.65Å/s and 6.0Å/s. While many of the results on this series of samples were given prior to this Subcontract period [3,4], additional and potentially important new results on this series of samples were obtained during the current Subcontract as well.

Indeed, the new results on these samples helped motivate a new set of studies involving several different research groups within the amorphous silicon Team. In addition to BP Solar and the University of Oregon, this collaboration included the University of North Carolina

(Daxing Han), the Colorado School of Mines (Don Williamson), and NREL (Brent Nelson). These studies employed a new series of samples from BP Solar for which the growth rates were 1Å/s, 3Å/s, 5Å/s and 10Å/s.

Films for our measurements were deposited onto smooth TCO coated glass with thicknesses ranging between 1.5 to 1.8 microns as determined by Dektak profiling. Matched p-i-n devices were fabricated in a glass/SnO_2/p/i/n/ZnO/Al structure (specular SnO_2) using the identical series of growth conditions. For the devices the i-layer thickness was kept close to 0.25μm. Simultaneous light-soaking treatments of the films and devices were carried out at the University of Oregon.

Films were also simultaneously deposited onto textured TCO coated glass for photoluminescence measurements carried out by Daxing Han. She also measured electroluminescence and IR absorption. Films were also co-deposited onto Al-foil substrates so that Don Williamson could carry out SAXS measurements. Finally, CPM measurements were carried out by Brent Nelson and his collaborators at NREL, using films co-deposited onto bare glass substrates.

All of the films and devices were characterized in their as-grown state (State A) and a subset were characterized in a light-degraded state (State B). The light-degraded state was obtained by illuminating the films and devices for 100 hours using the same red-filtered ELH light source at an intensity of 100 mW/cm^2. In degrading the films we were careful to compensate for the partial transparency of the Pd contacts.

2.4 NREL HOT-WIRE CVD AMORPHOUS SILICON-GERMANIUM ALLOYS

A series of seven a-Si,Ge:H samples deposited using the hot-wire CVD process with Ge fractions of 0, 15, 29, 47, 63, 81, and 100at.% were obtained from Yueqin Xu and Harv Mahan at NREL. These 1.2 to 1.6 micron thick alloy films were deposited onto n^+ a-Si:H coated stainless steel at substrate temperatures that varied during deposition – typically between 200°C at the beginning to an average of 290°C at the end. Tauc gaps ranged between 1.65eV for the 15at.% alloy sample to 0.98eV for the a-Ge:H endpoint film. More details are given in Table II. These films were deposited using a Ta filament that was operated a lower temperature (≤1800°C) than the NREL HWCVD a-Si,Ge:H samples we have studied in the past (those were deposited with a tungsten filament wire at temperatures of at least 2000°C). A semi-transparent Pd contact was thermally evaporated on top of the intrinsic layer to provide a Schottky junction for our capacitance based measurements.

TABLE II. Characteristics of HWCVD a-Si,Ge:H films obtained from NREL. All samples were deposited on n^+ a-Si:H coated Stainless Steel substrates. The substrate temperature at the beginning of each a-Si,Ge:H layer deposition was 200°C.

Sample	Thickness (μm)	Ge fraction (at.%)	T_{sub} at end (°C)	Dep. Rate (Å/s)	E_{04} (eV)	E_{Tauc} (eV)
L1304	1.75	0	309	1.62	1.90	1.74
L1305	1.50	15	295	1.39	1.79	1.65
L1306	1.60	29	293	1.78	1.66	1.50
L1307	1.44	47	292	2.00	1.47	1.32
L1308	1.38	63	286	2.56	1.40	1.22
L1309	1.15	81	275	3.14	1.28	1.12
L1310	1.18	100	279	3.27	1.05	0.98

Unlike the a-Si,Ge:H alloys examined by SAXS previously, including those produced by the glow discharge (PECVD) process, the HWCVD grown alloys deposited under these conditions exhibited roughly an order of magnitude lower SAXS signals for Ge fractions ranging from 20 to 80%.[5,6] This is particularly surprising given that moderate ion bombardment of the growing film, long thought to be essential for the production of high quality, dense a-Si,Ge:H film, is totally absent in the HWCVD growth process.

2.5 IOWA STATE AMORPHOUS GERMANIUM

We obtained a couple a-Ge:H samples prepared in Vikram Dalal's laboratory at Iowa State University that were depostion using their ECR growth technique. These samples were deposited in a "half-device" sample configuration: SS/n^+/a-Ge:H. The a-Ge:H films were deposited at 260-270°C with a H_2:GeH_4 dilution ratio of 100:1.[7] The a-Ge:H film thickness was 0.3μm. Our test devices were completed by depositing Cr Schottky barrier contacts on the top surface.

Initially we had some difficulty identifying a metal for the top contact that would lead to a good Schottky barrier. Our usual choice for a-Si,Ge:H alloy samples in the past was Pd; however, these did not produce good blocking contacts. Ultimately, we found that Cr contacts produced usable, but somewhat leaky, Schottky barriers. An admittance scan (capacitance and conductance vs. temperature) is displayed in Fig. 2(a). This set of data reveals a well-defined junction capacitance; however, the conductance is rather large at all frequencies. This means that some extra care needed to be taken to separate the capacitance and conductance phases of

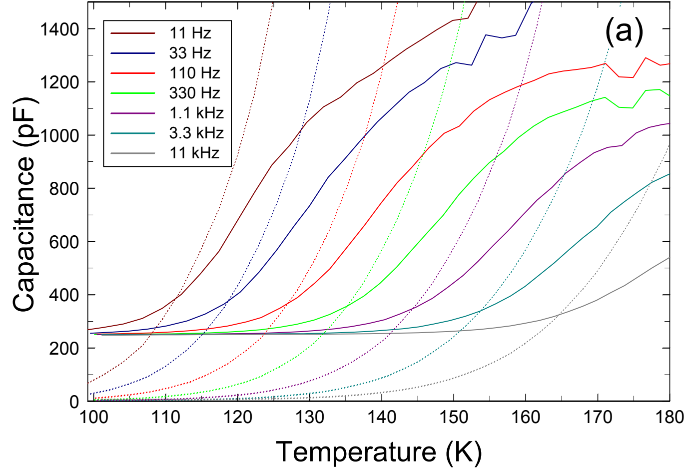

FIG. 2(a). Capacitance (solid lines) and conductance (dotted lines) vs. temperature for Iowa State a-Ge:H sample 6059 at 0V applied bias at seven measurement frequencies.

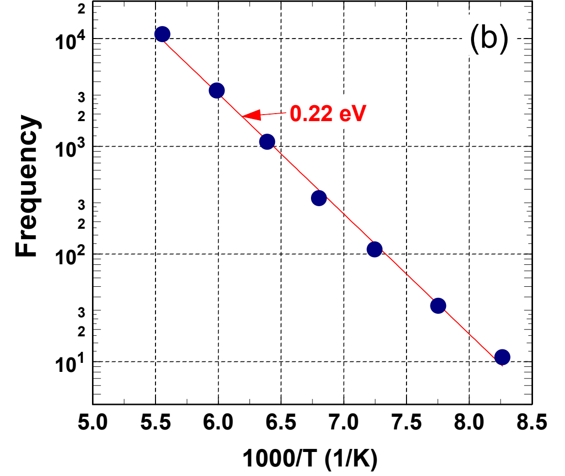

FIG. 2(b). Arrhenius plot of the inflection points of the capacitance step vs. frequency displayed in Fig. 1(a) reveals the activation energy of conductivity.

the current response. The step increase in the capacitance is thermally activated (see Fig. 2(b)) and discloses the conductivity activation energy for this a-Ge:H sample (about 0.22 eV).

3.0 EXPERIMENTAL CHARACTERIZATION METHODS

The measurements employed in our studies rely on a set of experimental techniques which have all been described previously in some detail. They consist of (1) admittance spectroscopy as a function of temperature and frequency, (2) drive-level capacitance profiling, and (3) transient photocapacitance taken together with transient junction photocurrent spectroscopy. Here we will describe each method only very briefly and review what kind of information is obtained from each type of measurement.

3.1 ADMITTANCE SPECTROSCOPY

Our Schottky diode samples contain a depletion region which is characterized as a function of temperature and frequency [see, for example, Fig. 2] before we undertake the more sophisticated capacitance based measurements described in Sections 3.2 and 3.3 below. Such measurements provide us with an estimate of our film thickness (the temperature independent region at low T is simply related to the geometric thickness, d, by the formula $C = \varepsilon A/d$), and an Arrhenius plot of the frequency of the lowest temperature capacitance step (or conductance peak) *vs.* 1/T provides us with the activation energy of the ac conductivity, E_σ, which we identify with the Fermi energy position: $E_\sigma = E_C - E_F$. [8] These admittance measurements also give us an indication of the quality of our Schottky barriers which allow us to pre-screen our samples for further study.

3.2 DRIVE-LEVEL CAPACITANCE PROFILING

The drive-level capacitance profiling method has been described in detail in many publications [9,10]. It is similar to other kinds of capacitance profiling in that it provides us with a density *vs.* distance profile; however, this particular method was developed specifically to address the difficulties encountered in interpreting capacitance measurements in materials with defect densities comparable to carrier densities. In this method we monitor the junction capacitance both as a function of DC bias, V_B, and as a function of the amplitude of the alternating exciting voltage, δV. One finds that to lowest order this dependence obeys an equation of the form:

$$C(V_B,\delta V) \quad = \quad C_o(V_B) + C_1(V_B)\,\delta V + \ldots$$

and that the ratio

$$N_{DL} \equiv \frac{C_0^3}{2q_e \varepsilon A^2 C_1} \tag{1}$$

is directly related to the free carrier density, n, plus an integral over the density of mobility gap defect states:

$$N_{DL} = n + \int_{E_c - E_e}^{E_F^o} g(E)dE \tag{2}$$

Here $E_F{}^o$ is the bulk Fermi level position in the sample and E_e depends on the frequency and temperature of measurement:

$$E_e(\omega,T) \quad = \quad k_B T \log(\nu/\omega) \tag{3}$$

Thus, by altering the measurement temperature (or frequency) we obtain information about the energy distribution of the defects and, by altering the applied DC bias, we can vary the spatial region at which we detect the defects in the sample. That is, we can spatially profile the defects as a function of the position from the barrier interface.

3.3 TRANSIENT PHOTOCAPACITANCE AND PHOTOCURRENT

The methods of junction transient photocapacitance and photocurrent have been discussed by us in great detail over the years in the literature [11,12,13,14] and also in previous NREL reports. They represent types of sub-band-gap optical spectroscopy and provide spectra quite similar in appearance to PDS derived sub-band-gap optical absorption spectra or to CPM spectra. Instead of detecting absorbed energy, however, our photocapacitance and photocurrent transient methods detect the optically induced change in defect charge within the depletion region.

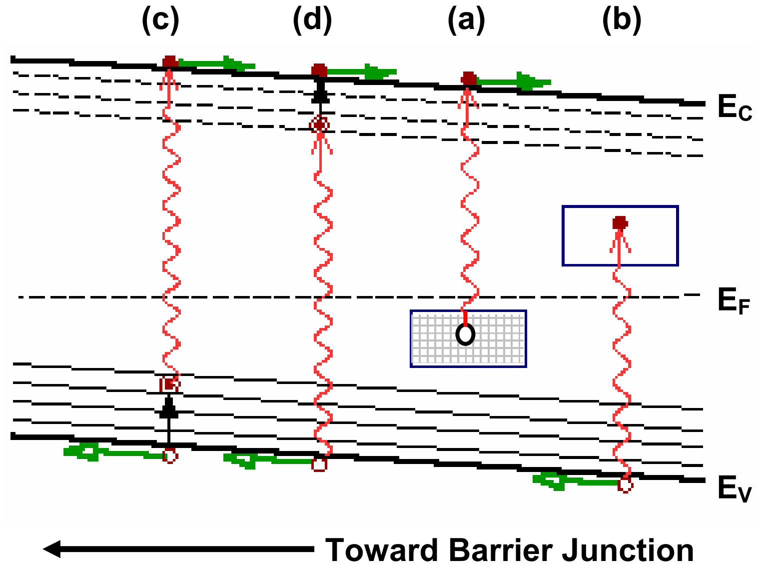

FIG. 3. Schematic of four different types of sub-bandgap optical transitions. Optical tran-sitions are shown by the wavy lines, and thermal transitions are shown by the vertical solid arrows. Horizontal arrows indicate the subsequent motion of the released carriers.

In this method the space charge region of the semiconductor near the barrier junction is first subjected to a voltage "filling pulse". This pulse causes a non-equilibrium (filled) occupation of gap states to be established. As time progresses, the initial steady-state population is recovered through the excitation of trapped electrons to the conduction band where they can then move out of the depletion region under the influence of the electric field. In the dark this process proceeds entirely by the thermal excitation of trapped carriers. However, this process can be enhanced through optical excitation and this is the basis of the photocapacitance and junction photocurrent techniques.

The re-equilibration can be observed by the redistribution of trapped carriers, either as a change in the *junction capacitance* (which occurs because the depletion region will contract as negative charge is lost and the positive charge density increases) or by monitoring the *current* which results from the motion of this charge. However, the observation of capacitance transients has one significant difference compared to current transient measurements: The dominant type of emitted carrier (electron or hole) can be identified by the *sign* of the observed change in capacitance.

Unlike the CPM method, both of our junction based techniques are not greatly influenced by the free carrier mobilities since, once an electron (or hole) is optically excited into the conduction (valence) band it will either totally escape the depletion region on the slow timescale of our measurement (0.1 to 1s) or be re-trapped into a deep state and not escape. In most cases

we assume that almost all of the optically excited majority carriers (electrons) *do* escape but, in general, only a fraction of the minority carriers (holes) do.

In Figure 3 we have separated the types of optical transitions involving gap states into four types. Type (a) is the removal of an electron from an occupied defect level into the conduction band with the subsequent escape of the electron. Type (b) represents the optical excitation between the valence band and an unoccupied defect states with the subsequent escape of the valence band hole. Such a transition results in a photocapacitance signal of negative sign. Generally, such negative photocapacitance signals occur only in very intrinsic material and are even fairly rare in those cases. They have been most prominently observed in some a-Si,Ge:H samples [15], and in some mixed phase a-Si:H / nc-Si:H samples [16].

Transitions of type (c) are similar to type (a) except that, because the hole left in the gap state lies close to the valence band, it will be quickly thermally emitted into the valence band where it then also escapes the depletion region. Such a case results in no change in charge state within the depletion and, hence, no photocapacitance signal. Similarly, [Type (d)] for a transition from the valence band into an unoccupied gap state close to the conduction band, the electron will be quickly thermally emitted into the conduction band and leave the depletion region as well, with nearly zero photocapacitance signal.

We expect that transitions of types (c) and (d) will be dominant when the photon energy lies only slightly below the bandgap energy. For such transitions each photon effectively produces one valence band hole plus one conduction band electron with no net change in the gap state occupation. However, we generally find that the photocapacitance signal in this energy regime does not vanish; rather, it is substantially *positive*. This thus indicates that photogenerated electrons are more likely to escape the depletion region than photogenerated holes. Moreover, while transitions of types (c) and (d) result in small changes in the junction capacitance, they result in a large junction photocurrent.

In general terms, if our sub-bandgap light results in n_e electrons and n_h holes leaving the depletion within the experimental time window, then the junction photocurrent signal will be proportional to $n_e + n_h$, while the photocapacitance signal will be proportional to $n_e - n_h$. Thus, it is really only by measurements of *both* the transient photocapacitance (TPC) signal *as well as* the transient photocurrent (TPI) signal that we can truly distinguish the quantities of holes and electrons excited out of the depletion region due to the sub-bandgap light.[14] This ability to distinguish electron from hole processes is unique among all the various types of sub-band-gap optical spectroscopies.

4.0 PROPERTIES OF UNITED SOLAR NANOCRYSTALLINE SILICON

Simple variations in the growth parameters used to deposit hydrogenated amorphous silicon (a-Si:H) result in the growth of a form of hydrogenated microcrystalline silicon with crystallite sizes less than 10nm: Hydrogenated nanocrystalline silicon, nc-Si:H. Such materials have been studied seriously for solar cell applications for over a decade [17]; however, only fairly recently have attempts to fabricate high efficiency a-Si:H/nc-Si:H tandem cells shown a reasonable degree of success.[18] Compared to a-Si:H, however, the range of materials called micro- or nano-crystalline silicon is enormous. Not only is there the important variable of crystallite size, but also issues such as the degree of a-Si:H contained between the crystallites, the role of hydrogen in passivating grain boundaries, oxygen contamination [19], and the variation of these properties as a function of film thickness [20] are expected to play a crucial role in determining the electronic properties of these materials. We have begun an effort to understand this class of materials. The specific goals include identifying the active defects and understanding their effects, characterizing the carrier densities and transport properties, and identifying under what conditions such materials may exhibit types light-induced degradation similar to a-Si:H. In the studies reported here, we will discuss results using admittance spectroscopy, drive-level capacitance profiling, and transient photocapacitance studies on the three samples obtained from United Solar Ovonic Corporation that were described in Section 2 above.

4.1 ADMITTANCE AND DRIVE-LEVEL CAPACITANCE PROFILING STUDIES

It had been found that nc-Si:H films were susceptible to post-deposition oxygen contamination which could be prevented by depositing capping layers of a-Si:H. Thus, we requested for study an initial sample (14140) that was a 3-layer sandwich consisting of a 700nm

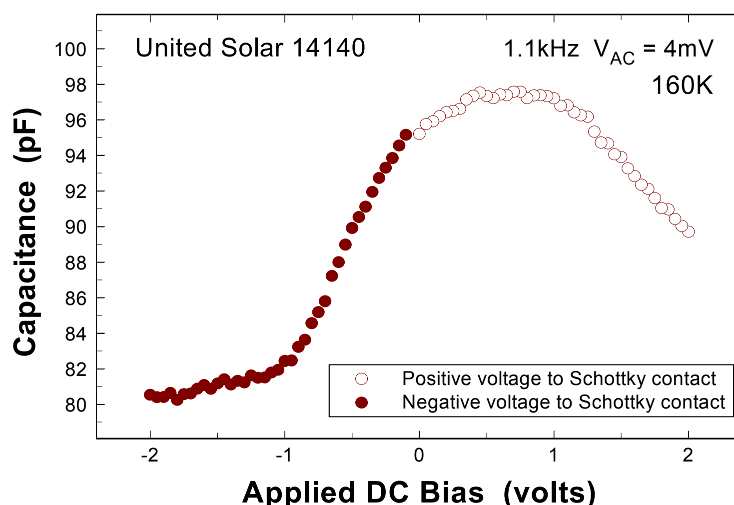

FIG. 4. Variation of the junction capacitance with voltage for the 14140 a-Si:H/nc-Si:H/a-Si:H sandwich sample. These data indicate that blocking contacts probably arise from the a-Si:H/nc-Si:H interfaces on both sides of the nc-Si:H layer. The asymmetry indicates that the effective “built-in potential” is different for the two interfaces. The CV variation is consistent with a doping density close to 10^{15} cm^{-3}.

thick nc-Si:H layer clad between two 200 to 250nm thick a-Si:H layers in a SS/n+/a-Si:H/nc-Si:H/a-Si:H structure. We finished our test devices by depositing a Pd Schottky barrier contact on the top surface. In Fig. 4 we display a capacitance voltage measurement for this sample device extending over both forward and reverse biases. We observe that, in spite of the n^+ contacting layer at the substrate, that we actually have blocking contacts for both polarities. We suspect that this behavior occurs as a result of the a-Si:H/nc-Si:H interfaces on both sides of the nc-Si:H layer. The CV dependence indicates an effective doping level of roughly 10^{15} cm^{-3}.

In Fig. 5(a) we display the variation of capacitance with temperature at +0.5V applied bias for a series of seven measurement frequencies. We can see that there are two prominent features: First, there is a large capacitance step lying between 200 and 300K (depending on the frequency). The frequency *vs*. temperature of the inflection point of this capacitance step exhibits Arrhenius behavior as is shown in Fig. 5(b). Initially we thought that this large capacitance step was due to the activation of conduction of the nc-Si:H material. However, the fact that the capacitance below this step varied with applied bias (see Fig. 5) contradicted this interpretation. That is, if conduction in the nc-Si:H became frozen out then we would simply observe a bias independent geometric capacitance at temperatures below the step. We therefore believe that, rather than indicating a deep defect level, the capacitance step most likely indicates the onset of participation of states at the nc-Si:H/a-Si:H interfaces to the capacitive response.

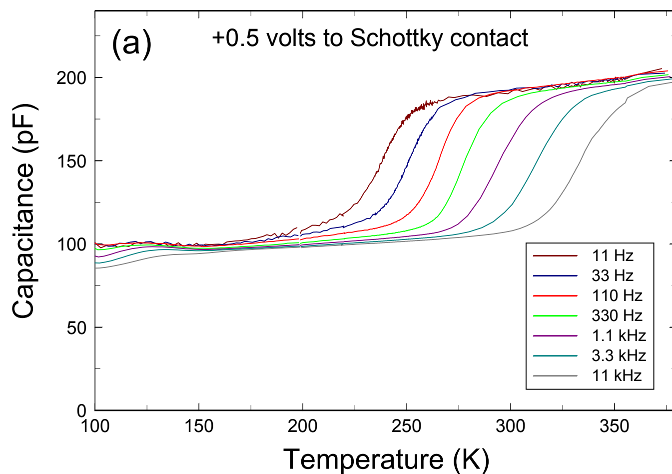

FIG. 5(a). Capacitance vs. temperature for a-Si:H/nc-Si:H/a-Si:H multilayer sample 14140 at +0.5V applied bias and seven measurement frequencies. Note the large capacitance steps at intermediate temperatures (230K to 320K) and the smaller capacitance steps below 130K. The latter is due to dielectric freeze-out of the nc-Si:H layer.

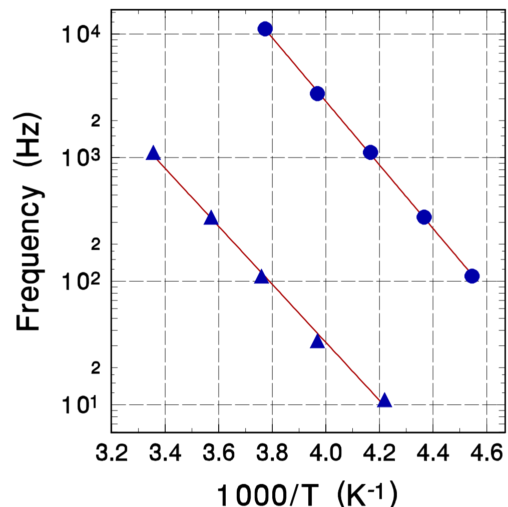

FIG. 5(b). Arrhenius plot of the large capacitance step vs. frequency displayed in Fig. 6(a) (triangles) reveals an activation energy near 0.5eV, close to half the nc-Si:H bandgap We obtain nearly the same activation energy, but very different prefactor, for the p-i-n nc-Si:H sample (circles).

Such an interface state response will often exhibit an activation energy of half the gap, particularly if it arises primarily from minority carrier trapping at such interfaces [21].

We obtained a very similar capacitance step and activation energy for the p-i-n sample 12123 as well [see Fig. 5(b)]. This tends to confirm our interpretation of the step since the thermal generation of carriers will be the same as for the sandwich sample, but the prefactor would be expected to be quite different since it would depend on the density and character of states located in this case at the p-i and/or the n-i interfaces.

The capacitance value in the intermediate temperature region in the sandwich sample is slightly below 100pF, and this corresponds to a total depleted width of roughly 0.9µm. We believe this corresponds to the two a-Si:H layers (roughly 0.5µm) plus a depleted region inside the nc-Si:H layer (of roughly 0.4µm). Below a temperature of roughly 130K we note that the capacitance exhibits another step. Although it is not clear what the asymptotic capacitance value will reach below this step, it appears that it will lie at or slightly below 80pF. This would correspond to a thickness of 1.15µm, or roughly the total thickness of all three layers. Thus, we believe the lowest temperature capacitance step exhibited in Fig. 5(a) actually corresponds to the dielectric freeze-out of conduction in the nc-Si:H layer itself. We note that this appears to occur at quite a low temperature compared to a-Si:H.

We next characterized these samples using the drive-level capacitance profiling (DLCP) technique. A series of 3.3kHz drive-level profiles for the pin sample device is shown in Fig. 6, and indicates densities near the mid 10^{15} cm^{-3} level. However, the variation of these densities

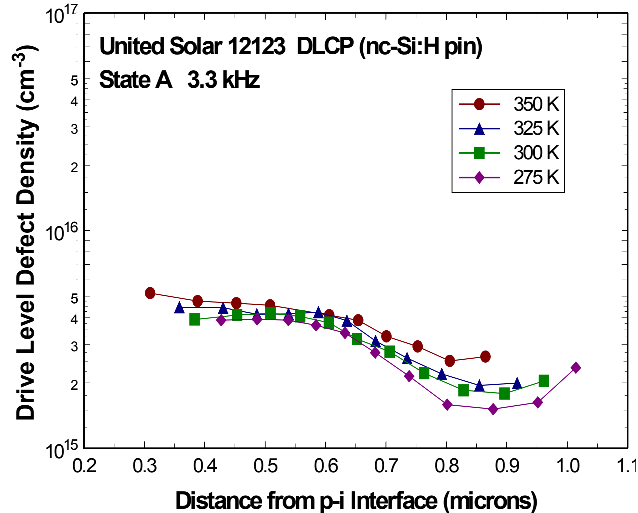

FIG. 6. DLCP curves for the p-i-n nc-Si:H device. Note the small variation of these curves with temperature which indicates that the responding states are relatively shallow.

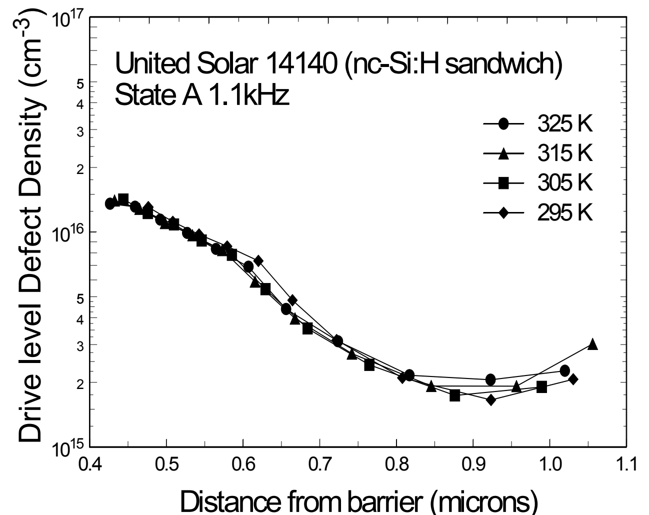

FIG. 7. DLCP curves for the a-Si:H/nc-Si:H/a-Si:H multilayer sample showing a similar qualitative behavior to that of the p-i-n device.

FIG. 8. Drive-level capacitance profiles for nc-Si:H deposited under conditions of hydrogen profiling. Unlike the DLCP profiles for the samples deposited under constant hydrogen dilution shown in Figs. 6 and 7, these profiles reach a maximum and then start decreasing again as the film continues to grow.

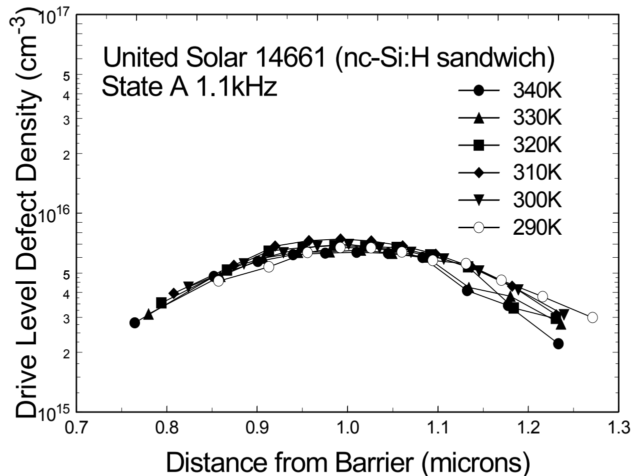

with temperature is quite small. This suggests that the majority of the responding states are shallow donor-like states, lying within about 0.55eV of the conduction band. A small component of deeper defects may be indicated by the *difference* between the high and low temperature profiles. For this sample we see that any deeper defect density appears to be much less than 1 x 10^{15} cm^{-3}. A similar series of drive-level profiles is displayed in Fig. 7 for one of the multilayer samples (without hydrogen profiling). These appear to be qualitatively quite similar to those of the pin device except that they indicate a density perhaps twice as large as those for the pin device. This spatial variation is present in all 3 samples deposited under constant hydrogen dilution and is believed to result from the increase in crystalline volume fraction and size as the film growth progresses. In contrast, when hydrogen profiling is employed to control the nanocrystalline evolution, as shown in Fig. 8, the sample exhibits a DLCP profile that reaches a maximum value $\leq 10^{16}$ cm^{-3} within the middle of the film before decreasing again toward the front surface. We note that hydrogen profiling also results in an increase of efficiency of solar cells [5], which seems to be a direct consequence of the reduced defect density.

4.2 SUB-BAND-GAP PHOTOCAPACITANCE SPECTROSCOPY

In Figures 9 and 10 we display two types of sub-band-gap spectra. The first, in Fig. 9, is a high signal quality CPM spectrum for hydrogenated microcrystalline silicon (μc-Si:H) taken from the literature [22]. The second, in Fig. 10, is a set of transient photocapacitance (TPC) spectra, taken at three different measurement temperatures, for one of the United Solar nc-Si:H sandwich sample devices. It is quite striking that, at the lowest measurement temperature (180K), the TPC spectrum appears quite similar to the CPM spectrum for μc-Si:H, while at the highest measurement temperature (280K), the TPC spectrum appears very similar to what one would expect for hydrogenated *amorphous* silicon!

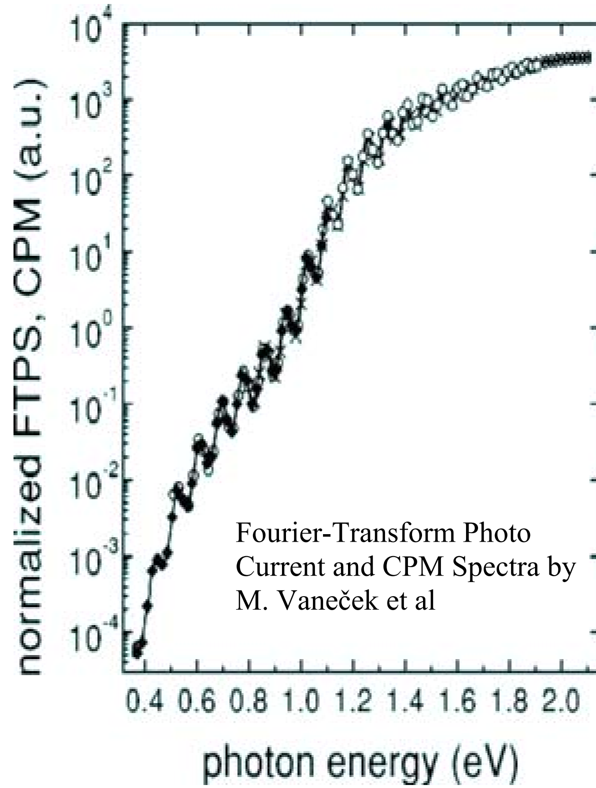

FIG. 9. CPM spectrum for μc-Si:H taken from the paper by M. Vaneček et al [22]. Note the high signal-to-noise (S/N) at low photon energies that was achieved by employing Fourier transform spectrometry.

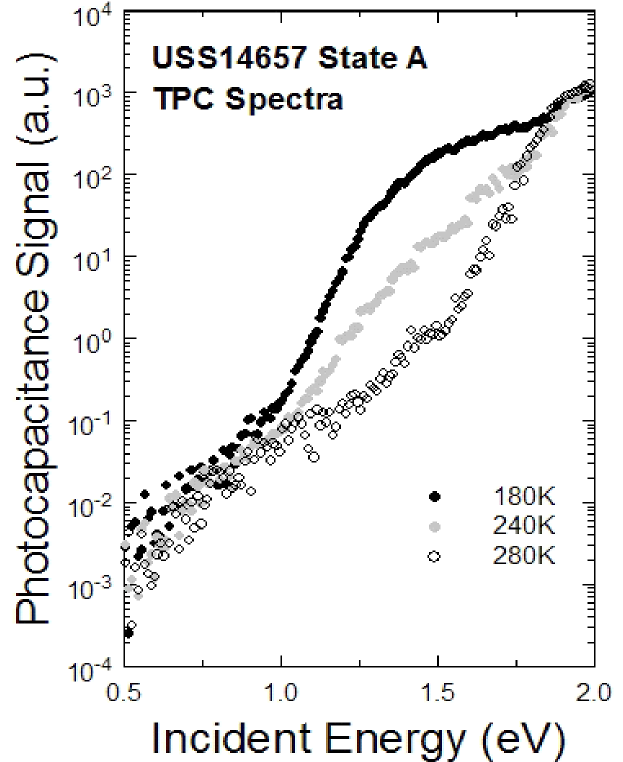

FIG. 10. TPC spectra for one sandwich nc-Si:H sample device at three measurement temperatures. Note that at 180K the spectrum appears very similar to that for μc-Si:H shown in Fig. 9 with similarly good S/N. However, at 280K the spectum appears similar to sub-band-gap spectra for a-Si:H.

We believe that the variation in the appearance of the TPC spectra indicates the mixed phase nature of the United Solar nc-Si:H material. Specifically, we believe that the evolution of the appearance of these spectra from being more μc-Si like at lower temperatures to more a-Si:H like at higher temperatures is due to the suppression of the signal component from the nanocrystallites when a majority of minority carriers is able to escape the depletion region during the photocapacitance measurement time window. This cancels the charge change (and hence the photocapacitance signal) caused by the escape of the optically excited majority carriers that is dominant at the lower temperatures. (See the discussion in Section 3.3 above). In contrast, more of the minority carriers generated in the amorphous silicon component of the sample appear to remain trapped and so this component of the sample dominates the spectrum above 280K.

Figure 11(a) displays the TPC spectra for a second sandwich sample device at two temperatures, while Fig. 11(b) shows the TPI spectra at the same two temperatures. We again observe the more a-Si:H-like spectrum at the higher measurement temperature for TPC. However the TPI spectra appear nearly the same and quite μc-Si-like at all temperatures. This

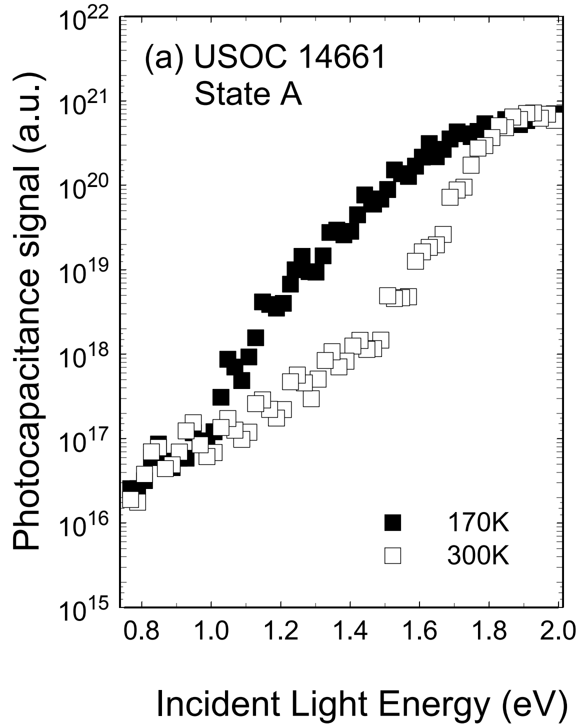

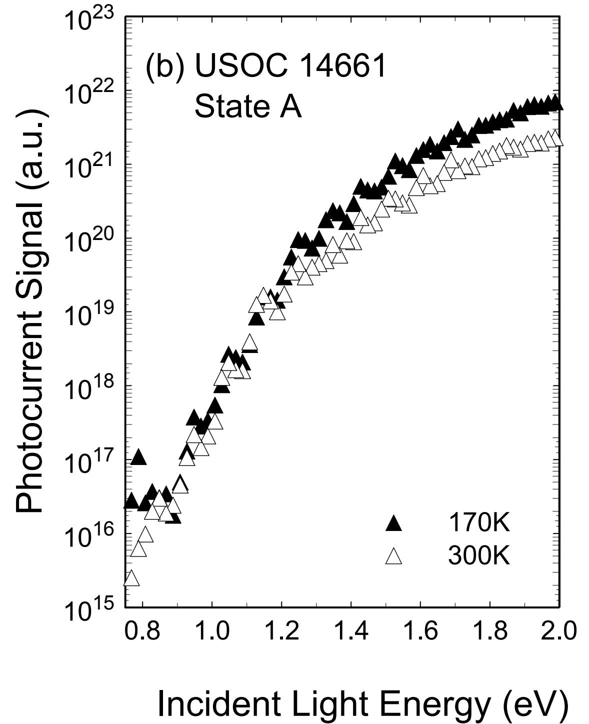

FIG. 11(a). Photocapacitance spectra for the hydrogen profiled a-Si:H/nc-Si:H/a-Si:H multilayer sample at two measurement temperatures. The a-Si:H component dominates at higher temperatures because the nanocrystallite component signal is suppressed due to its higher minority carrier fraction.

FIG. 11(b). Transient junction photocurrent spectra for the same temperatures as shown in Fig. 11(a). Here the minority carrier collection adds to rather than cancels the signal. Thus, the spectra are dominated by the majority nanocrystalline component at all temperatures.

FIG. 12. Photocapacitance spectra for the pin nc-Si:H device at two similar temperatures to those employed for the measurements of the sandwich sample device shown above. Since the pin device contains no a-Si:H capping layers, this proves that the more a-Si:H appearance at higher temperatures comes from its presence within the nc-Si:H material itself.

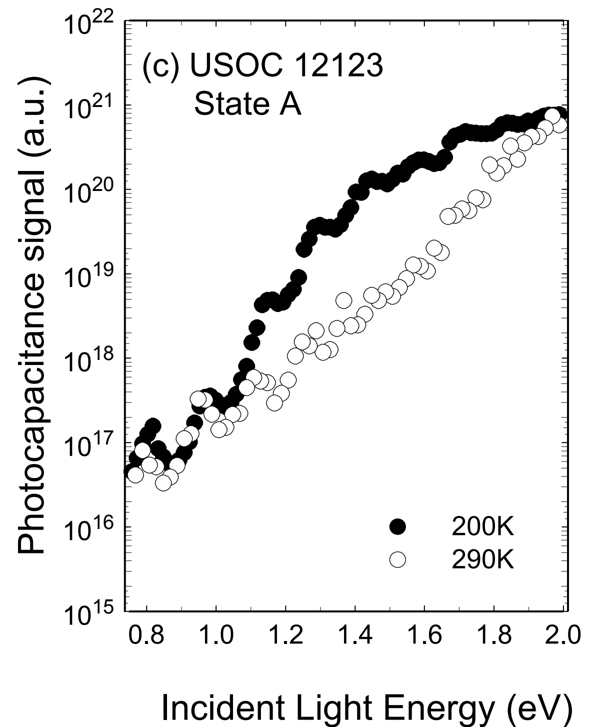

confirms our interpretation that it is the suppression of the TPC signal in the nanocrystalline component due to increased minority carrier collection that is responsible for the temperature variation in the photocapacitance spectra. Conversely, because any such increased minority collection will only enhance, rather than suppress, the TPI signals, these spectra appear nearly μc-Si-like at all temperatures since that component is the dominant one.

Initially we were unsure whether the a-Si:H component seen for the sandwich samples came from the nc-Si:H layer itself or from the a-Si:H layers of the multilayer devices. The latter possibility did not seem likely at these low measurement temperatures since the conductivity in the a-Si:H layers would be too low to respond to a kHz oscillating voltage. In Fig. 12 we display TPC spectra at two similar temperatures for the nc-Si:H p-i-n device (12123) that contains no a-Si:H layers. We see that these spectra appear qualitatively similar to the TPC spectra for the sandwich samples shown in Figs. 10 and 11 except that the Urbach energy is larger, about 80 meV (possibly due to some increased oxygen contamination in this sample). This therefore confirms that the a-Si:H component of these spectra arises because the United Solar nc-Si:H material is a composite containing a significant fraction of a-Si:H. This conclusion has recently been verified by XRD measurements on similar United Solar nc-Si:H films.[23]

We examined the temperature dependence of the TPC signal for sample 14657 (see Fig. 10) in some detail, by recording its magnitude near 1.5eV as the temperature was varied between 170K and 300K. The result is shown Fig. 13, and indicates that the hole collection is *thermally activated*, with an activation energy of 0.22eV. This activation energy may imply the existence of a hole trap within the nc-Si:H component of these materials with an energy barrier for the release of holes near 0.2eV.

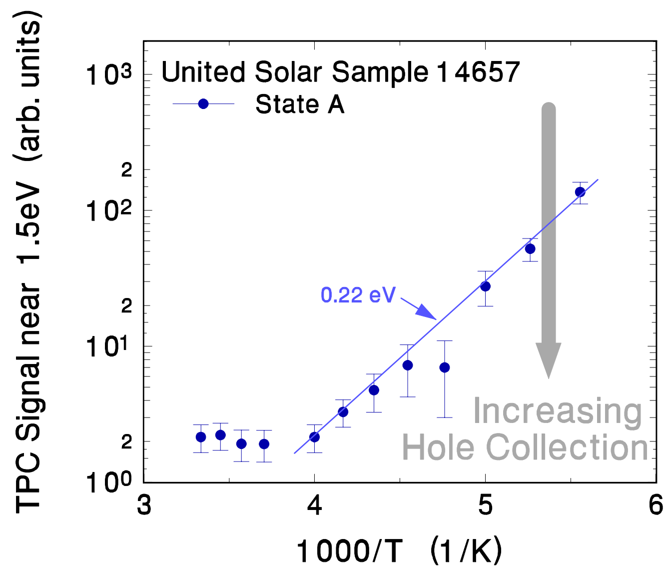

FIG. 13. Temperature dependence of the TPC signal near a 1.5eV optical energy (see Fig. 10). The smaller the magnitude, the larger the hole collection in the nanocrystallite component. The temperature dependence appears thermally activated, perhaps due to a specific hole trap within the nc-Si:H material. The limiting value in the higher temperature region indicates the magnitude of the signal arising from the amorphous silicon component.

4.3 LIGHT INDUCED EFFECTS IN NANOCRYSTALLINE SILICON

Although it has been reported that microcrystalline Si is largely immune from the light induced degradation effects exhibited by a-Si:H [24,25], recent studies on the performance of nc-Si:H solar cell devices fabricated at United Solar [26] have revealed a several percent loss in efficiency, depending on the deposition conditions, after prolonged exposure. On the other hand, nearly no change in properties is seen in our admittance or drive-level profiling measurements. In Fig. 14 we display the results of drive-level capacitance profiling (DLCP) measurements on sandwich sample 14140 in State A, and after 1, 3, 10, and 30 hours of light soaking. These profiles indicate that very little has changed in the electronic properties of this sample. We note, however, that under the experimental conditions employed (1.1kHz and 320K) these measurements would only be sensitive to defect states shallower than about 0.60eV. Therefore, we would miss any response from deeper states, such as dangling bond defects within the a-Si:H component.

The photocapacitance spectra, on the other hand, *do* indicate significant changes due to light-soaking. In Fig. 15 we compared three TPC spectra for sandwich sample 1467: The annealed state spectrum at 240K and 180K, as well as a light soaked state ("State B") obtained by exposure to red (>610nm) filtered ELH light at an intensity of 100 mW/cm^2 for 100 hours. Here we see quite clearly that light induced degradation has reduced the hole collection by almost exactly the same amount as reducing the temperature in the annealed state of this sample from 240 K to 180 K.

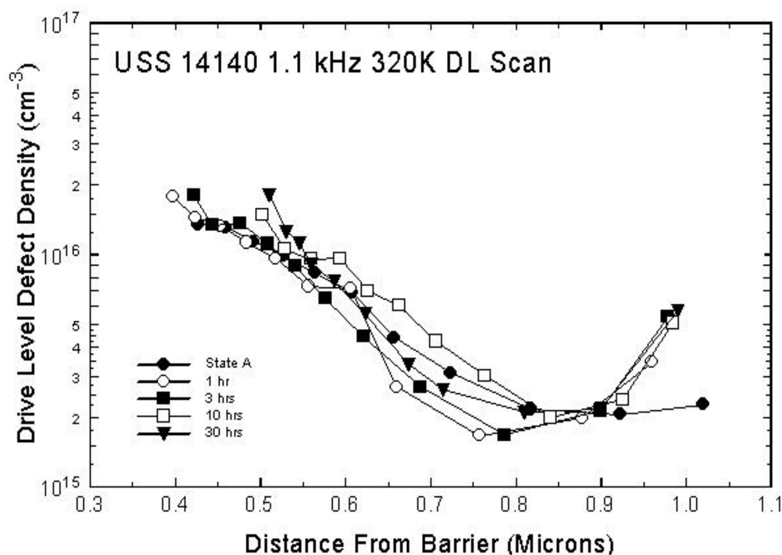

FIG. 14. Drive-level capacitance profiles taken at 1.1kHz and 320K for State A and the various stages of light soaking indicated. These densities exhibit only relatively minor changes with light exposure which are likely due to minor changes in the interface change density rather than the nc-Si:H material itself.

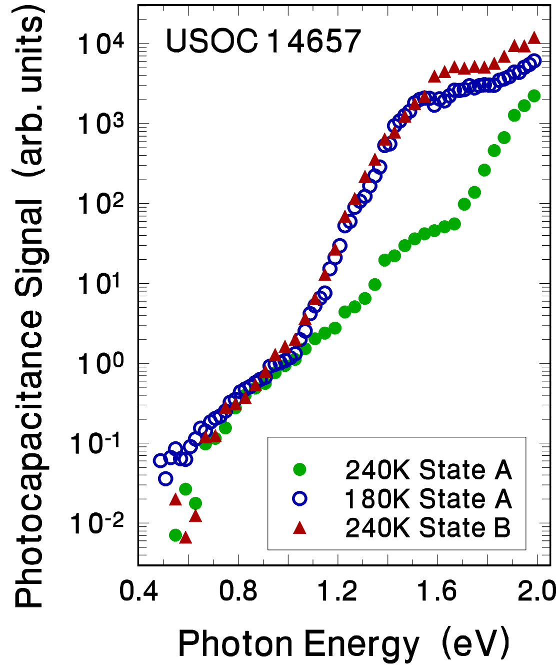

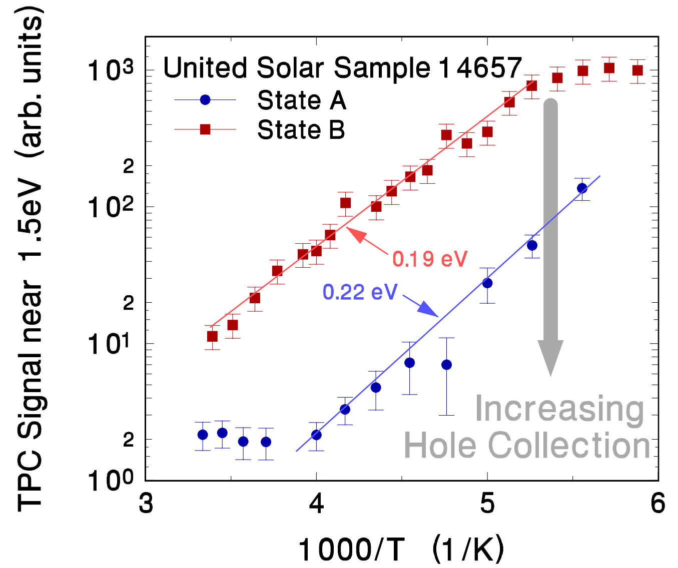

FIG. 15. Comparison of TPC spectra in State A at 180K and 240K, along with the TPC spectrum at 240K after prolonged light exposure (State B). In the last case the hole collection is reduced to a level comparable to that of State A at 180K.

FIG. 16. Detailed temperature dependence in State A and State B of the TPC signal magnitude near 1.5 eV. The fraction of holes collected appears thermally activated with nearly the same energy in both cases, but is more than 10 times higher in State A over a wide temperature range (180-250K).

Again we examined the temperature dependence of the TPC signal in more detail for photon energies near 1.5 eV. This temperature dependence is plotted in Fig. 16 and is compared with the corresponding behavior in the annealed state. Here we observe a TPC signal that is more than 10 times larger at all temperatures, indicating a significantly decreased hole collection in State B compared to State A. Note that in both the high and low temperature extremes the TPC signal does reach a limiting value; specifically, that determined by the a-Si:H signal component in the high temperature regime, and a maximum value corresponding to negligible hole collection in the low temperature regime. It is interesting that the slopes (activation energies) are only slightly different between State B and State A.

The loss in hole collection does not appear to be linked to an increase in deep defects. In Fig. 17 we display a series of 180 K and 280K spectra for a series of metastable states for the same sample following a series of partial isochronal anneals after light exposure. At 180K temperature the fraction of holes collected during the TPC time window is quite small and these spectra thus appear essentially identical. In particular, there is no change in the deep defect

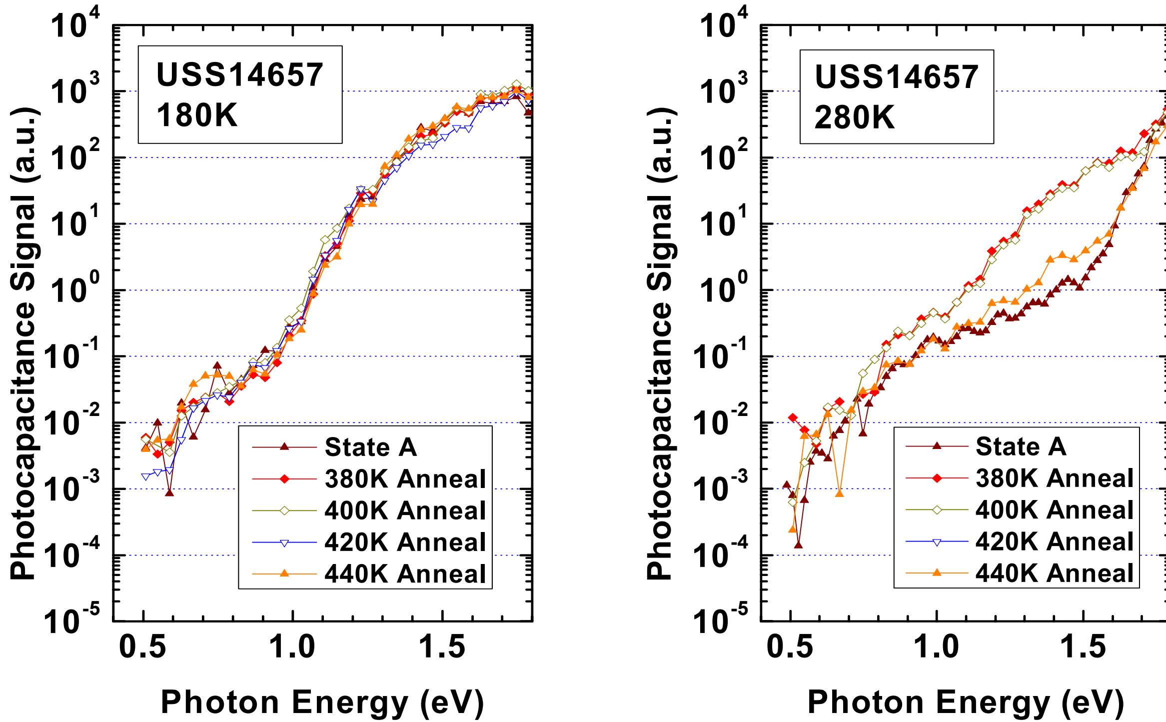

FIG. 17. TPC spectra at two measurement temperatures for a series of metastable states produced by partial annealing a fully light soaked state at the temperatures indicated. Note that there is no evidence for any differences in the deep defect portion of these spectra (the region at photon energies less than 1 eV).

magnitude of these spectra within the measurement uncertainty. However, the TPC spectra obtained at 280 K for the same sequence of partial anneal states indicate a change in the fraction of holes collected by nearly a factor of 50 while, at the same time, indicating no difference within the experimental uncertainty in the defect band portion of the spectra. Therefore, this implies an entity other than the deep (dangling bond) defects must be dominating the light-induced degradation in these samples.

5.0 UNITED SOLAR AMORPHOUS SILICON NEAR PHASE BOUNDARY

As described in Section 2.2, near the beginning of this Subcontract period, we obtained a couple of samples from United Solar Systems to explore the variation of properties above and below the transition to microcrystalline growth. These samples are largely amorphous in the central regime but, as one moves radially outward, become more amorphous (see Fig. 1). Thus, using one such sample film one can, in principle, explore properties ranging from nearly pure amorphous, through a mixed phase regime, to almost purely microcrystalline.

For our studies we deposited an array of 1mm diameter Pd dots over the film surface. Unfortunately, however, to date these types of contacts resulted in robust Schottky barrier

devices only for the portion of the film that was nearly in its purely amorphous phase. Thus, we have not been able to study the properties of this sample through its transition as we had hoped. On the other hand, we did manage to characterize the properties of the most amorphous portion in both its dark annealed (state A) and light degraded state (state B). A series of drive-level profiles we obtained for each of these metastable states for one particular Schottky device are displayed in Fig. 18.

In State A we found a defect density almost too small to measure in this 2μm thick film. That is, the increasing defect density beyond the 1.8μm position is almost certainly due to the fact that the edge of the depletion region is running into the n+ layer at the substrate. Thus, a rough estimate of the defect density would come from doubling the value of the 360K, 33Hz profile near 1.75μm where the profile begins to flatten. This gives 1.0 x 10^{15} cm^{-3}.

After light soaking the depletion region becomes significantly smaller and this allows much more accurate profiles and densities to be probed. In this case we double the 350K, 11Hz to estimate the total deep defect density. A very low degraded value of 6 x 10^{15} cm^{-3} is obtained, and the sample properties appear to be quite spatially uniform.

FIG. 18(a). Drive-level profiles for a region near the center of film L13698 in its dark annealed state. We believe that the best estimate of the deep defect density is obtained from doubling the value of the 360K profile near 1.75μm.

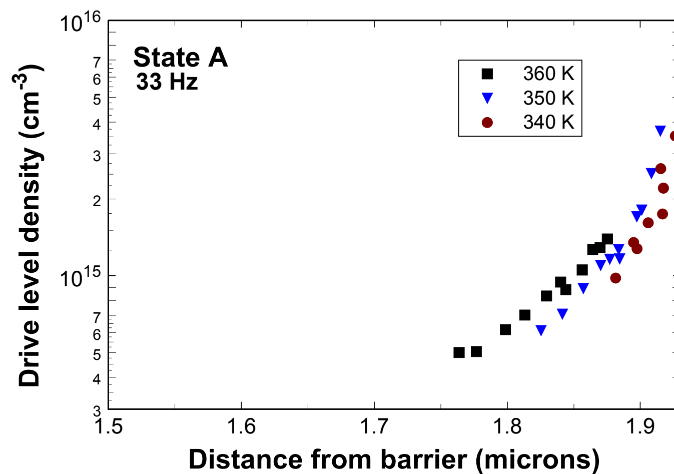

FIG. 18(b). Drive-level profiles for the same region of film L13698 after degrading by light soaking it for 100hours at an intensity of 1W/cm^2 (using a red filtered ELH light source). In this case very uniform profiles are obtained. We estimate a deep defect density of 6 x 10^{15} cm^{-3}.

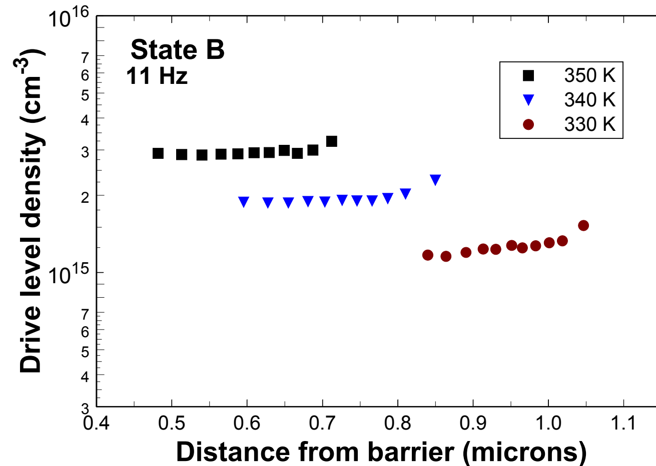

6.0 BP SOLAR HIGH GROWTH RATE AMORPHOUS SILICON SAMPLES

6.1 REVIEW OF PREVIOUSLY REPORTED RESULTS

In a collaborative study with Gautam Ganguly while he was at BP Solar, we had examined DC glow discharge a-Si:H samples whose depostion rate was varied by changing the hydrogen dilution or discharge power levels. The first series of studies examined six samples whose growth rates varied between 0.65Å/s to 6Å/s. Matching solar cell devices for these films were characterized at BP Solar. Both the films and devices were characterized in their as-grown states (State A) and a degraded state (State B) using the identical light source (red-filtered ELH light at an intensity of 100mW/cm^2 for 100 hours). In degrading we were careful to compensate for the partial transparency of the Pd contacts deposited on the films for our junction capacitance based measurements.

As we reported under our previous NREL Subcontract XAF-8-17619-05 [3], there was a clear inverse relation between the device performance and the growth rate for this series of samples [Fig. 19(a)]. Also as reported previously, and shown in Fig. 19(b), there was essentially *no correlation* between the defect densities in these samples for either state A or state B, and the growth rate. The fact that the magnitude of the deep defect density determined by DLCP was nearly constant, independent of growth rate in both state A and state B, was quite a surprising result given the clear monotonic variation in device performance. It prompted our further characterization of these films using transient photocapacitance spectroscopy (TPC). The TPC technique essentially yields an optical absorption spectrum with a very high sensitivity. A pair of typical TPC spectrum for one film in states A and B is shown in Fig. 20(a). Such spectra

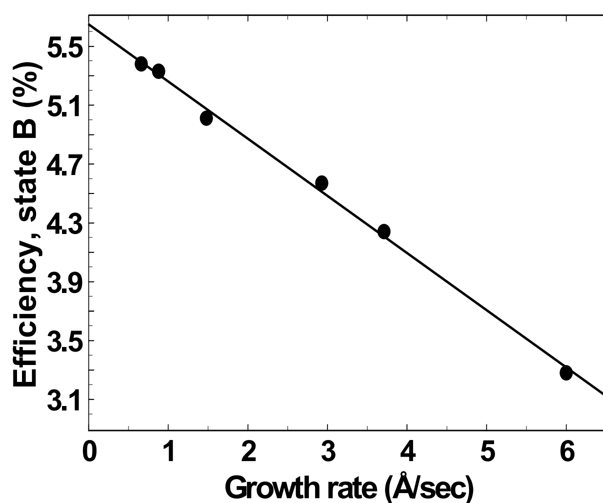

FIG. 19(a). A monotonic loss of device efficiency in the degraded state is observed with increasing growth rate (From Ref.3)

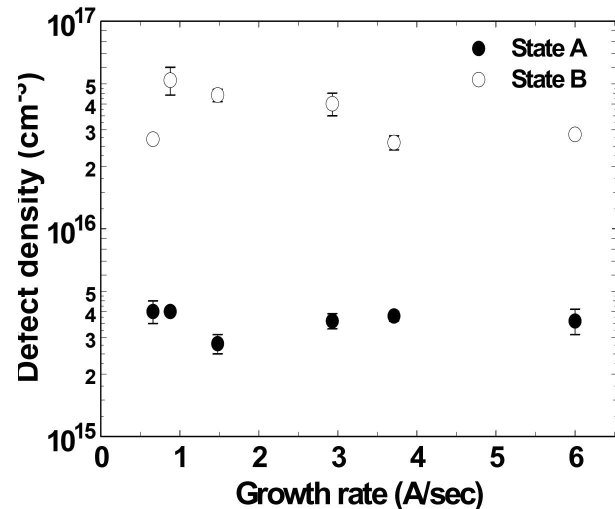

FIG. 19(b). Defect densities obtained from DLCP measurements are roughly independent of growth rate for both state A and the light-degraded state B (From Ref. 3).

are well fit using a combination of a gaussian band of deep defects plus an exponential band of tail states. An example of such a fit to one photocapacitance spectrum is shown in Fig. 20(b).

As also reported under our previous Subcontract, the Urbach energies determined from these spectra *did* correlate reasonably well with growth rate such that higher growth rates exhibited broader band tails. The dependence of Urbach energy with growth rate is shown in Fig. 21. The broadening of the bandtail is not too surprising given that void densities are known to increase substantially for glow discharge samples as the deposition rate increases. On the other hand, it then seemed surprising to us that the deep defect densities did *not* seem to increase with the increasing value of the Urbach energy given the predicted relationship between the two from defect equilibration models.

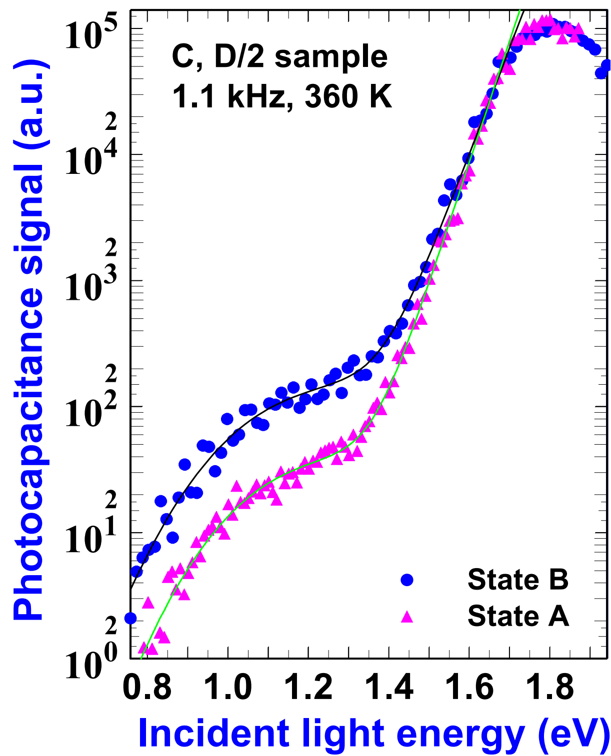

FIG. 20(a). Photocapacitance spectra for a 1.5Å/s growth rate sample in both the annealed state and the light-degraded state.

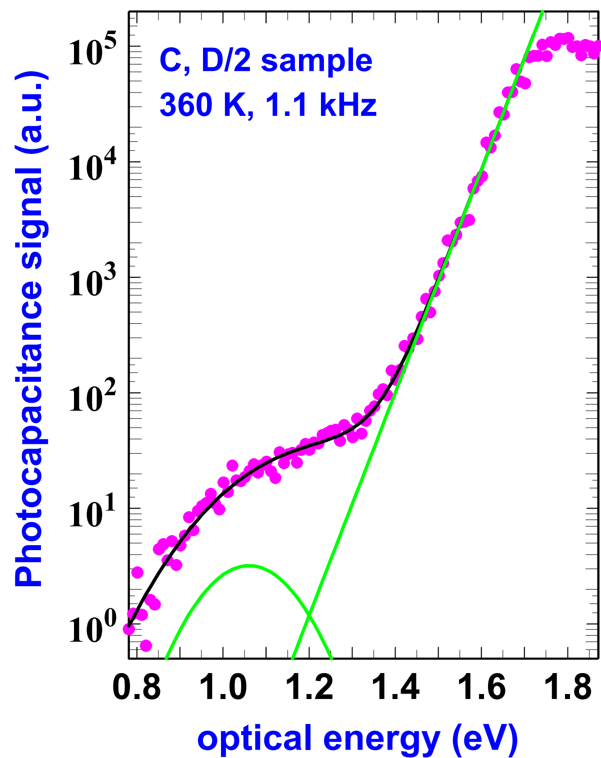

FIG. 20(b). Example of how spectra are fit with an exponential bandtail plus a Gaussian shaped defect band. We deduce relative deep defect magnitudes for different samples by aligning these spectra at the optical gap (E04) energy.

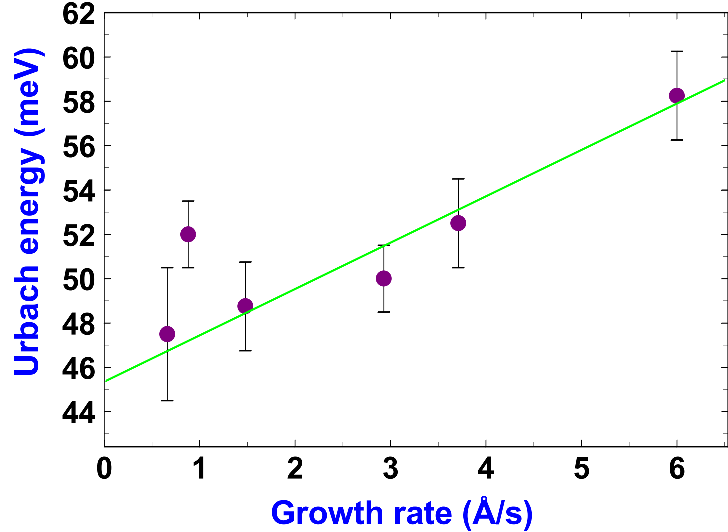

FIG. 21. The Urbach energies deduced from the photocapacitance spectra correlate fairly strongly with the sample growth rates.

6.2 CORRELATION BETWEEN DEFECT DENSITIES AND DEVICE PERFORMANCE

During the first year of Subcontract ADJ-2-30630-17 we decided to examine more closely whether there might be a correlation between the magnitudes of defect density determined via our sub-band-gap spectra and device performance. Indeed, while the deep defect magnitudes determined from DLCP remain nearly constant across this series of samples (Fig. 19b), the defect band revealed in the sub-band-gap photocapacitance spectra *does* seem to exhibit a fairly strong dependence on growth rate. To compare the defect band signals for different samples we have scaled the TPC results to have an identical magnitude at the optical (E_{04}) gap. This then allows us to estimate relative values for the deep defect band magnitudes contained in the gaussian band. [see Fig. 20(b)]

It is important to note that, in several previous studies of a-Si:H using DLCP together with TPC, it has been demonstrated that both methods give essentially identical results for both the magnitude and energy distribution of the deep defect band (except that the optical energies are perhaps 80meV larger compared to the corresponding thermal activation energy determined by DLCP).[27] However, the TPC derived defect densities for these samples, in contrast to the DLCP results, actually do seem to correlate quite well with device performance, as is illustrated in Fig. 22(a). The TPC defect densities for state A and state B appear quite closely linked as well, as shown in Fig. 22(b). A summary of the Urbach energies and deep defect densities deduced by the DLCP measurements in both states A and B, along with the relative defect magnitudes deduced by the TPC measurements are summarized in Table III.

This series of companion thin film and device samples thus appears to have provided a valuable testing ground for previously proposed relationships between E_U, deep defect density, and device performance. Indeed, to our knowledge this was the first report of a strong

correlation between E_U, the state B defect density, and the device performance.[See Section 10, Publ. 3] We've noted that defect densities and device performance are most closely correlated in state B. This may be expected since materials properties are likely to dominate in the highly degraded state while, in state A, characteristics such as the quality of the junctions and interfaces may be more important limiting factors. On the other hand, two of the samples in state A have very good device performance, but exhibit TPC determined defect densities nearly as large as some state B samples [the points lying farthest off the line in Fig. 22(a)]. While we are currently unable to offer an explanation for this, it is interesting to note that these are the two samples deposited with the lowest degree of hydrogen dilution for this series of samples.

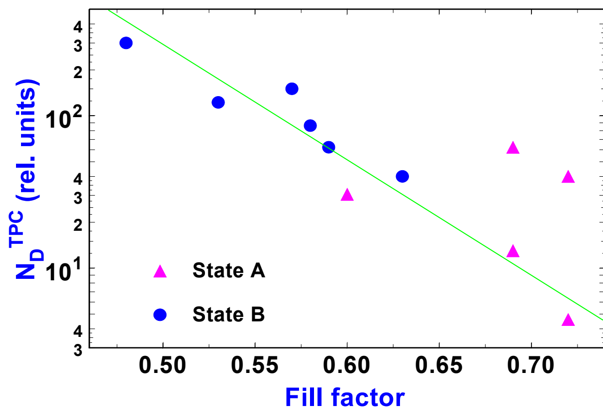

FIG. 22(a). Magnitude of deep defect band deduced from TPC spectra vs. matched device fill factor. Correlation is quite strong, particularly in the light degraded state.

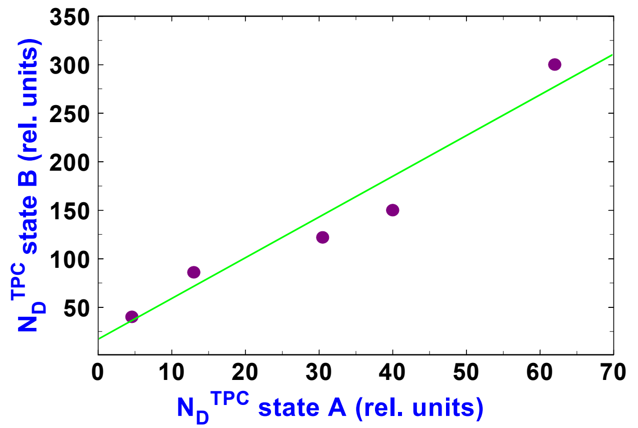

FIG. 22(b). Defect band magnitudes determined from TPC spectra in states A and B are related by nearly a constant factor.

Table III. Film results for samples in the annealed state (State A) and after light soaking (State B) are listed in order of increasing growth rate. These include defect densities obtained from drive level capacitance profiling (N_D^{DLCP}) and from transient photocapacitance spectroscopy (N_D^{TPC}).

				State A		State B	
Growth Rate (Å/s)	Relative Discharge Power	Relative Hydrogen Dilution	E_U (meV)	N_D^{TPC} (a.u.)	N_D^{DLCP} (cm^{-3})	N_D^{TPC} (a.u.)	N_D^{DLCP} (cm^{-3})
0.66	C	2D	48	4.6	4.0×10^{15}	40	2.7×10^{16}
0.88	C	D	52	--	5.4×10^{15}	62	6.8×10^{16}
1.5	C	D/2	49	40	2.8×10^{15}	150	4.4×10^{16}
2.9	5C	D	50	13	3.6×10^{15}	86	4.0×10^{16}
3.7	5C	2D	53	31	3.8×10^{15}	120	2.6×10^{16}
6.0	5C	D/2	58	62	3.6×10^{15}	300	2.5×10^{16}

Thus a very puzzling aspect of the data presented above is the large difference between the defect densities determined by the DLCP method, which do not appear to be correlated to the device performance, and those determined by the TPC spectra, which definitely are. Also, we have noted that previous studies, which applied both types of measurements to the same samples, generally indicated good agreement between the defect densities determined by the two methods[27]. In this case there is a marked difference; indeed, the DLCP defect densities hardly vary with growth rate at all! A lack of correlation between deduced deep defect densities in films and performance of matched devices has also been noted in several other studies.[28,29,30] However, in nearly all of those cases the deep defect densities were estimated using the constant photocurrent method (CPM).

One appealing possible explanation is that the *intrinsic properties* of the deep defects are changing with growth rate in a manner that is reflected in TPC but not the DLCP or CPM measurements. For some time researchers (particularly at Penn State University) have been suggesting an important role for charged metastable defects.[31] This was to account for the observed magnitude of device degradation compared to the modest densities of metastable defects disclosed by CPM measurements. Charged defects, with their presumably much larger carrier capture cross sections, would lead to higher carrier recombination rates and poorer device performance.

Such an explanation might be invoked for our results as well, particularly when we note that deep defects with larger optical cross sections would appear larger in magnitude for TPC spectra, *but not for CPM*. This is because any increase in cross section, if it affected both emission and capture, would cancel out of CPM (since it is a steady-state method), but definitely enhance the optically induced carrier emission rate detected by TPC. Thus, a significant increase in the fraction of charged versus neutral deep defects with growth rate could account for our results. An alternative hypothesis to an increased density of charged defects might be that the deep defects in higher growth rate material have larger carrier cross sections because they reside near voids or in more strained environments. Indeed, it is well known that increased growth rate leads to a higher microvoid density in glow discharge samples.

6.3 STUDIES ON NEW SERIES OF BP SOLAR HIGH GROWTH RATE SAMPLES

Motivated in part by the results reported in Section 4.2, Gautam Ganguly organized a larger scale collaboration to investigate the detailed change in properties of the BP Solar DC glow discharge samples as the growth rate was increased. A new series of samples was produced using four different growth rates ranging from 1Å/s to 10Å/s (see Section 2.1). The series of

TABLE IV. Summary of cell parameters in State A for matched BP Solar devices.

Sample	Growth Rate (Å/second)	V_{OC} (volts)	J_{SC} (mA/cm^2)	FF	Efficiency (%)
L2127	1	0.89	11.26	0.71	7.16
L2129	3	0.90	10.72	0.72	6.96
L2136	5	0.89	10.70	0.68	6.49
L2137	10	0.90	9.41	0.67	5.65

studies on these samples involved a five way collaboration among BP Solar, the University of Oregon, University of North Carolina (Daxing Han), School of Mines (Don Williamson), and NREL (Brent Nelson).

The electronic properties of the films deposited onto the TCO coated glass were characterized by junction capacitance measurements at the University of Oregon, and included measurements the deep defect densities, electrical conductivities, and sub-band-gap photocapacitance spectra. The textured TCO coated glass films were sent to Daxing Han for photoluminescence, electroluminescence, and IR absorption. Films were also deposited onto bare quartz substrates and are intended for future ESR measurements to determine neutral dangling bond densities. Aluminum foil substrate films were characterized by SAXS measurements by Don Williamson. Finally, a set of films were deposited onto bare glass substrates and were prepared for CPM measurements by depositing Cr coplanar contacts. Those CPM measurements were carried out by Brent Nelson and his collaborators at NREL.

Both the films and devices were characterized in their as-grown state (State A) and a subset were characterized in a light-degraded state (State B). The light-degraded state was obtained by illuminating the films and devices for 100 hours using the same red-filtered ELH light source at an intensity of 100 mW/cm^2. In degrading the films we were careful to compensate for the partial transparency of the Pd contacts. Cell performance parameters were determined in both States A and B by Gautam Ganguly at BP Solar. The cell results determined by Gautam are for State A are summarized in Table IV. For State B device efficiencies are roughly 1% lower than for State A. As had been determined for a previous series of BP Solar devices, there appears to be a clear inverse relation between the device performance and the growth rate.

The defect densities determined by DLCP for all four films is quite low, and appears reasonably uniform except at the largest profiling distances (within 1000Å of the substrate – see Fig. 23 for a representative set of profiles for one sample). However, this apparent increase in

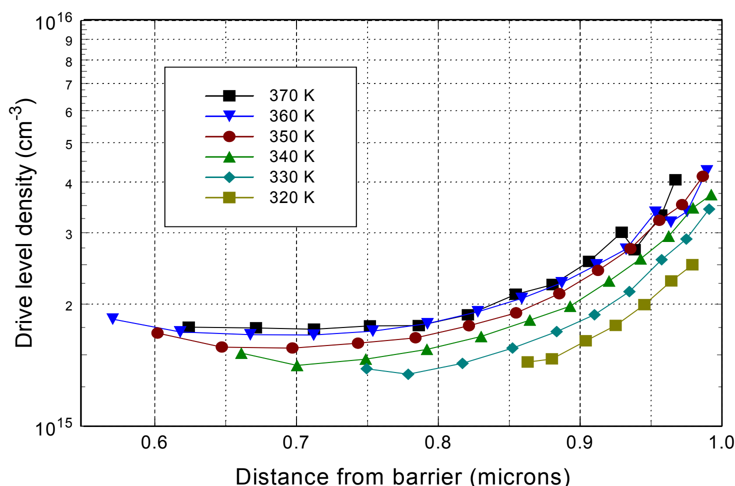

FIG. 23. Drive-level capacitance profiles for sample L2129 (3Å/s) in the dark annealed state. The measurement frequency was 11Hz for all temperatures. The total deep defect density is estimated by doubling the (spatially averaged) DLCP density at 360K. This would result in an estimated deep defect density in this case of 3.5 x 10^{15} cm^{-3}.

the profiles at large distance may actually be caused by the fact that the edge of the depletion region is running into the edge of the film at the substrate.

In Figure 24 we plot the DLCP defect densities obtained for all 4 samples in this series as a function of growth rate, both for State A and State B. In both states we see that the DLCP defect density does not vary in any clear way with growth rate (and hence neither with the device performance). This is consistent with our DLCP results for the previous set of BP Solar samples discussed in Section 6.1 above.

Next we determined the sub-band-gap spectra of these samples using transient photo-capacitance spectroscopy. Two such spectra for the lowest growth rate sample (L2127) in State A are displayed in Fig. 25(a) (these two spectra were taken under different values of reverse bias to test for spatial dependence of the electronic properties). For this 1Å/s growth rate sample the

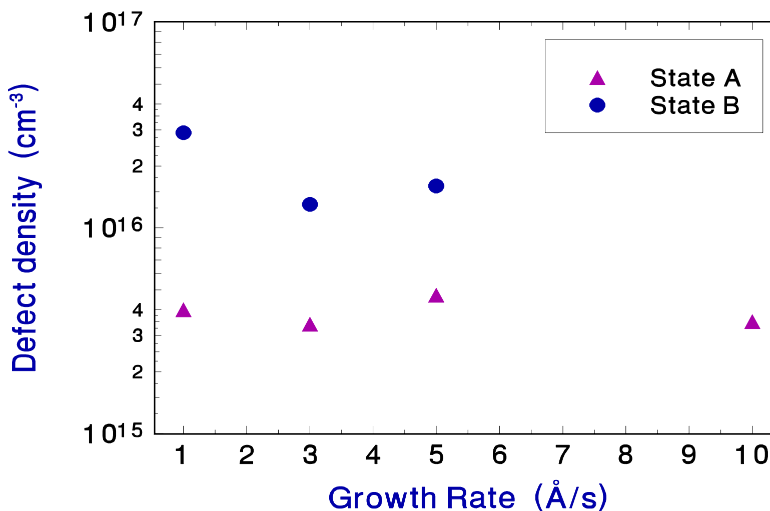

FIG. 24. Deep defect densities vs. growth rate for BP Solar films for both States A and B. These defect densities are estimated by *doubling* the 11Hz, 360K DLCP values. As with the results on a previous series of BP Solar samples, there appears to be little correlation between the deep defect density and the growth rate.

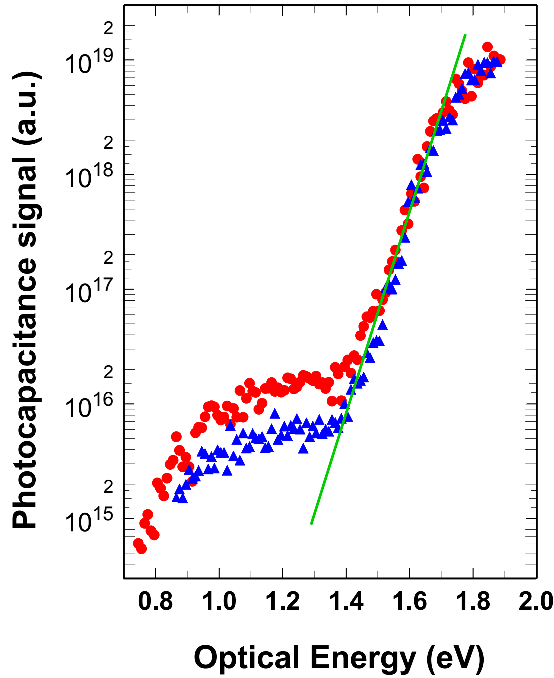

FIG. 25(a). Photocapacitance spectra for sample L2127 (1Å/s) taken at 380K at two values of reverse bias: -3V (circles) and –1V (triangles). Thus these data indicate a higher defect density near the substrate interface.

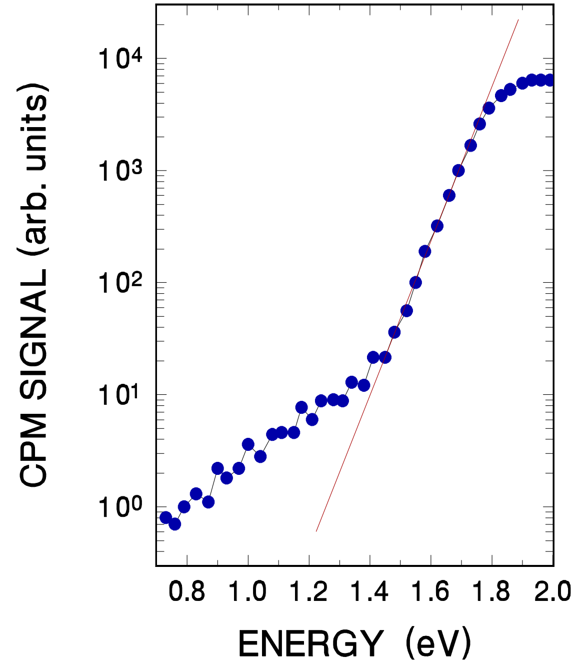

FIG. 25(b). CPM spectra obtained at NREL for the same sample. Note that the magnitude of the deep defect band is similar to the TPC spectra, but that the Urbach tail is much broader (61meV compared to less than 45meV for the TPC spectra).

Urbach tail is quite narrow – it has a characteristic energy of less than 45 meV. Because these samples were also examined using CPM spectroscopy at NREL, it is quite interesting to compare the results of our photocapacitance measurements with the corresponding CPM spectra. In Fig. 25(b) the corresponding CPM spectrum for this sample is shown, also for State A. We observe that both spectra indicate a similar deep defect density; however, the shapes of the defect band clearly differ. Also, the Urbach energy deduced from the tail distributions is markedly different: it exceeds 60meV for the CPM spectra. Such differences between these two types of sub-band-gap spectroscopy have been noted by us previously (for other sources of samples). It suggests to us that the CPM measurement reflects an additional broadening due to potential fluctuations over the transverse distance between the contacts. This could affect the secondary photocurrent signal which is the basis for the CPM measurements, but should not be an issue for the energy dependence of the transition rate that produces photocapacitance spectra.

For this series of 4 samples we found, in agreement with our results on the earlier BP Solar sample series, that the Urbach energies determined were correlated with growth rate such that

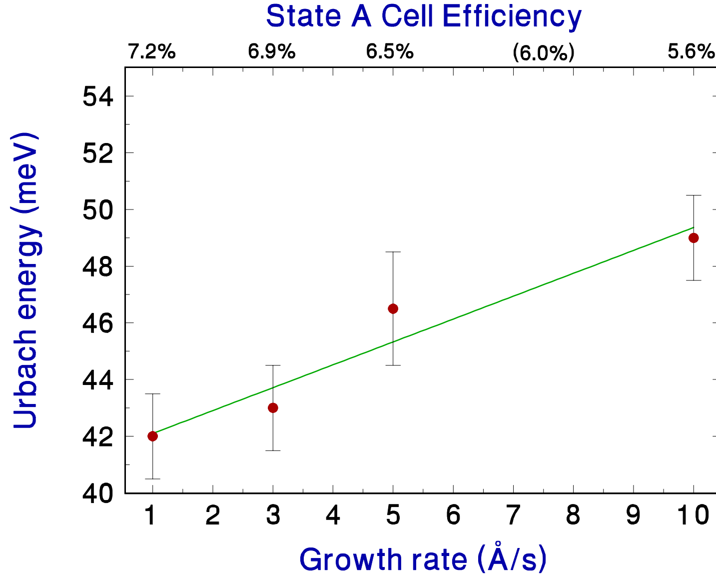

FIG. 26. Urbach energies determined from TPC spectra vs. film growth rate. These data suggest a reasonably strong correlation. Note also the matched device efficiencies for these growth rates indicated on the top scale.

higher growth rates exhibited broader band tails. The dependence of Urbach energy with growth rate is shown in Fig. 26. The matched device efficiencies are also indicated. In Table V, we compare the void fractions determined by Don Williamson and the hydrogen content determined at NREL with the Urbach energies we have obtained from our TPC measurements. We note that, in all cases, a clear trend is apparent. We have also included the CPM determined Urbach energies in this Table. These do *not* exhibit a clear trend with growth rate. Indeed, the CPM determined Urbach energies are always significantly larger than those determined by TPC.

TABLE V. Comparison of TPC determined Urbach energies with growth rate, as well as hydrogen content (NREL), void fraction (CSM), and CPM determined Urbach energies (NREL).

Growth Rate (Å/second)	Hydrogen (at.%)	Void fraction (volume %)	TPC derived Urbach energy (meV)	CPM derived Urbach energy (meV)
1	10.4	0.02	42.0±1.5	60.7
3	11.6	0.08	43.0±1.5	57.4
5	12.2	0.08	46.5±2.0	62.6
10	16.1	0.6	49.0±1.5	---

Finally, we tried to gain some additional insight into the factors that may be responsible for the decrease in cell performance from our TPC spectra. Previously we had demonstrated that a comparison between transient photocapacitance (TPC) spectra and junction transient photocurrent (TPI) spectra were quite valuable because one could estimate the fraction of photo-excited holes that were able to escape the depletion region on the time scale of the transient measurement window. This estimate is based on the fact that the holes that escape will reduce the TPC signal magnitude while enhancing the TPI magnitude. Unfortunately, recording the companion TPI spectra is not possible on our current test devices that employ Schottky barrier junctions due to the presence of an internal photoemission signal that partially masks the junction photocurrent signal.

To overcome this problem we attempted an alternative approach; namely, we recorded the TPC spectra at two different temperatures. Examples of such pairs of photocapacitance spectra are shown in Fig. 27. The idea was to effectively prevent the holes from escaping the depletion region during the 300ms measurement time window by deep trapping them at a lower temperature, then repeating the measurement at a higher temperature such that they could now escape the traps within that time window. In the latter case, however, recombination would still limit the number of holes escaping. For our initial attempt with this method we employed the

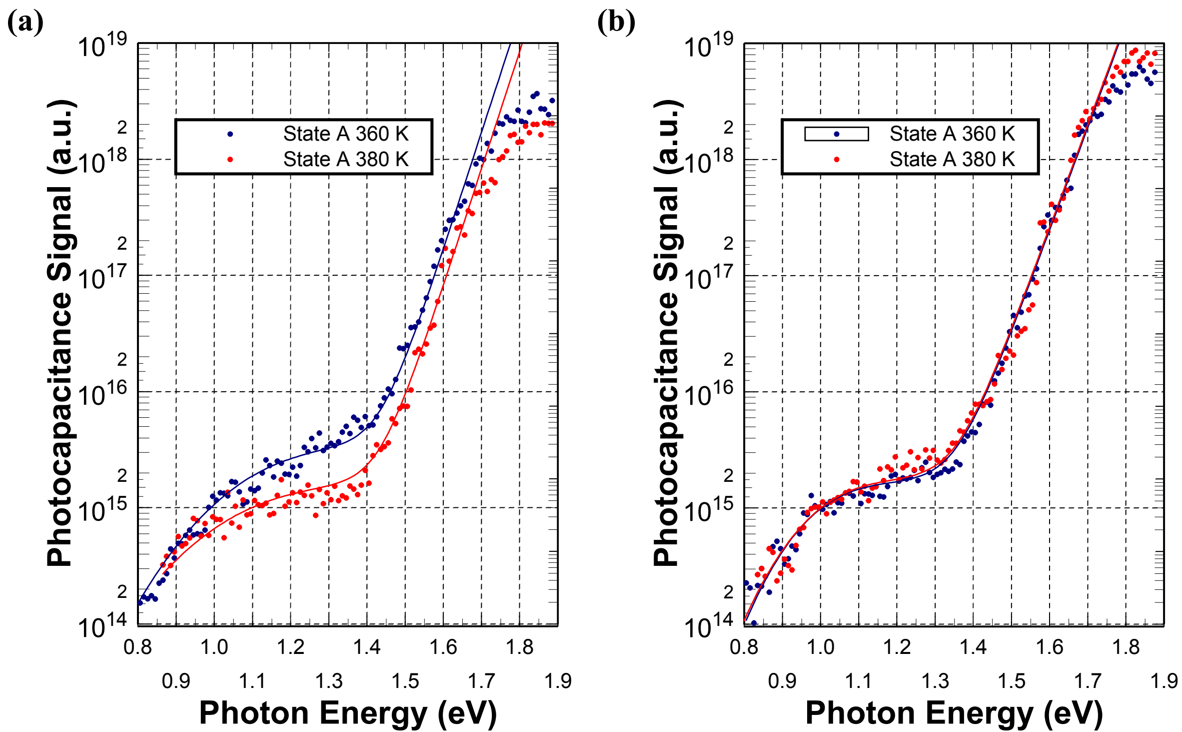

FIG. 27. Photocapacitance spectra for two BP Solar films in State A: **(a)** Sample L2127 deposited at 1Å/s, and **(b)** Sample 2137 deposited at 10Å/s. In each case the spectra have been recorded at two measurement temperatures: 360K and 380K. Note that there is a significant difference between the two spectra in (a), but not in (b).

temperatures of 360K and 380K which, for a 0.9eV deep dangling bond defect, imply thermal detrapping times of roughly 0.4s and 0.09s, respectively.

The spectra in Fig. 27 show that, for the data on the 1Å/s sample, there is a clear reduction in the TPC signal in the bandtail region for the higher temperature. This indicates that a significant fraction of holes (at least 65%) are able to escape the depletion region in 200ms at 380K. On the other hand, the spectra for the 10Å/s sample appear identical at both temperatures. This indicates that very few holes are collected even at 380K. We believe this reduction of hole collection may be an important clue in identifying the predominant mechanism for the loss in device performance for the higher growth rate samples.

In retrospect the choice of 360K and 380K as temperatures to estimate the hole collection efficiencies may not be optimal. Taking additional photocapacitance spectra over a larger range of temperatures could help to identify the best such temperatures to use for this purpose. In addition, we wish to check this approach using a-Si:H films deposited onto p^+ crystalline Si substrates so that TPI spectra may also be recorded. In this manner we hope to refine our approach so that we obtain the best possible estimates of the hole collection efficiencies for our "half device" test samples.

7.0 NREL HOT-WIRE AMORPHOUS SILICON-GERMANIUM ALLOYS

7.1 GENERAL ELECTRONIC PROPERTIES

Amorphous silicon-germanium alloys (a-Si,Ge:H) are a very important component for the production of the highest efficiency amorphous silicon based multi-junction & tandem solar cells. Unfortunately, optimized a-Si,Ge:H alloys using the RF Plasma Enhanced Chemical vapor deposition (PECVD) process require deposition at very low rates, typically less than 1Å/s. This translates into relatively high manufacturing costs. Efforts to increase the PECVD deposition rates without degrading the electronic properties have not yet been realized for these alloys. The hot wire chemical vapor deposition (HWCVD) method [32] has been shown to greatly increase the deposition rate (~16 Å/s as in [32]) of pure amorphous silicon without significantly degrading its electronic properties. However, several previous attempts to apply this method to the a-Si,Ge:H alloys have resulted in materials with poor electronic properties including, in particular, large deep defect densities and broad band tails. Examples of photocapacitance spectra for several HWCVD samples deposited at NREL prior to 2002 are shown in Fig. 28. We see that once the Ge fraction exceeded 20at.%, the electronic properties of these materials became quite inferior to those produced using standard PECVD growth methods, exhibiting Urbach energies in excess of 55meV and defect densities in the mid to high 10^{16} cm^{-3} range.

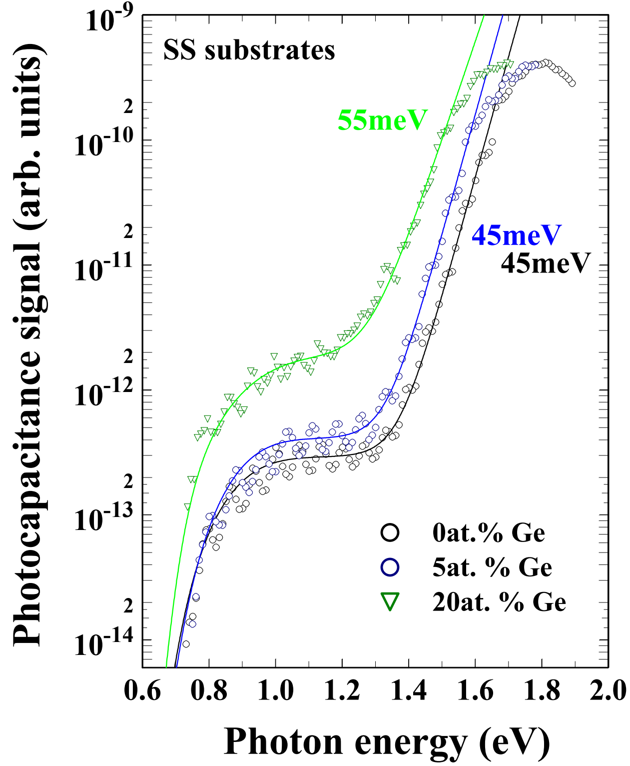

FIG. 28. Previous TPC spectra of NREL HWCVD alloy material [3] Although good electronic properties are seen for very low Ge, adding even 20at.% Ge leads to dramatically broader bandtails and higher defect densities.

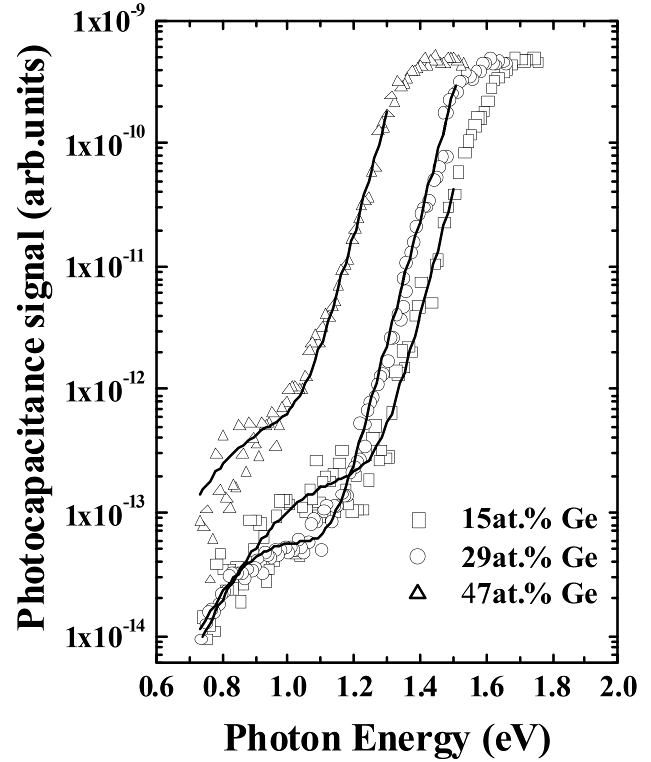

FIG. 29. TPC spectra of the low filament temperature HWCVD samples with 15 , 29, and 47at.% Ge. The samples were measured at 380K/1.1 kHz, at 380K/3.3 kHz and at 340K/80 kHz, respectively.

Recently, however, a variation of this technique using lower filament temperatures implemented at NREL (see Section 2.4) has shown considerable promise since it appears to lead to improved microstructure of the hot-wire a-Si,Ge:H alloys as revealed by small angle x-ray scattering (SAXS) studies [33,34]. In Fig. 29 we display TPC spectra for three such HWCVD a-Si,Ge:H samples of Ge fractions 15, 29, and 47at.%. Here we find much narrower bandtails and lower defect densities. By fitting these spectra to an exponential tail distribution plus a

Table VI. Summary low filament temperature HWCVD a-Si,Ge:H sample electronic properties.

Sample	Ge Fraction (at.%)	Growth Rate (Å/s)	E_{04} (eV)	E_{Tauc} (eV)	E_U (meV)	Defect Density (cm^{-3})
L1305	15	1.39	1.79	1.65	42 ± 2	2×10^{15}
L1306	29	1.78	1.66	1.50	43 ± 3	$4{\pm}2 \times 10^{15}$
L1307	47	2.00	1.47	1.32	45 ± 2	$2{\pm}1 \times 10^{16}$

FIG. 30. Drive-level capacitance profiling reveals very low midgap defect densities for the a-Si,Ge:H samples with Ge fractions of 15, 29, and 47at.%. These measurements were taken at 360K with frequencies of 110 Hz for the 15 and 29at.% Ge samples, and at 380K with 11kHz for the 47at.% sample.

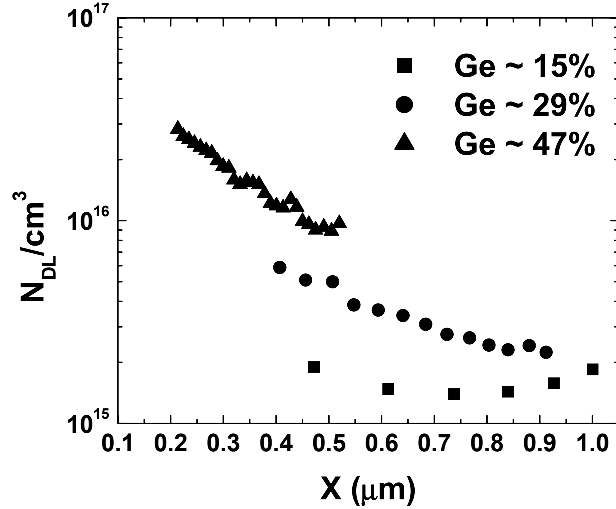

gaussian band of deep defects we have determined that all them have Urbach energies below 45meV. In addition, DLCP measurements on these three alloy samples displayed in Fig. 30 reveal defect densities below 10^{16} cm^{-3} for Ge fractions up to 30at.%. The characteristics determined for these three alloys samples are summarized in Table VI.

It is also evident from figure 30 that the defect densities gradually increase towards the junction interface. This probably reflects the fact that the substrate temperatures during the HWCVD growth was increased from 200°C to nearly 300°C as the film growth progressed. Therefore, we believe this is likely responsible for the higher defect densities disclosed near the barrier interface of the 29 and 47at.% samples.

Although the deduced lower defect density and narrower bandtails suggest that the current HWCVD alloys have superior electronic properties, the performance of solar cells crucially depends on the efficiency of the minority carrier collection in the device structure. We can try to estimate this by comparing the *ratio,* R, of the TPC and TPI spectra in the bandtail regime.

As has been discussed previously [14], if we align the spectra at low optical energies, along the deep defect bands, then this ratio R should be equal to $(1 - \eta)/(1 + \eta)$, where $\eta = n_h/n_e$ is the minority carrier collection efficiency and n_e, n_h are the respective numbers of photo-generated electron and holes leaving the depletion region. Previous studies [15] that examined this ratio in the best PECVD grown a-Si,Ge:H materials returned values of at least 10 or more. However, when we compare the TPC and TPI spectra of the 29at.% sample in Fig. 31, there appears to be essentially no difference. This suggests that the hole collection fraction is small. Similar results were obtained for the 15 and 47at.% samples. This is very surprising given the fact that all these alloys have very sharp band tails and low density of structural defects as described above. We are still searching for a suitable explanation for these apparently contradictory behaviors.

FIG. 31. Comparison of TPC and TPI spectra for the 29at.% Ge sample aligned at low optical energies. The fact that there is very little difference between the two types of spectra indicates that there is essentially no minority carrier collection being detected during the experimental time window (about 300ms).

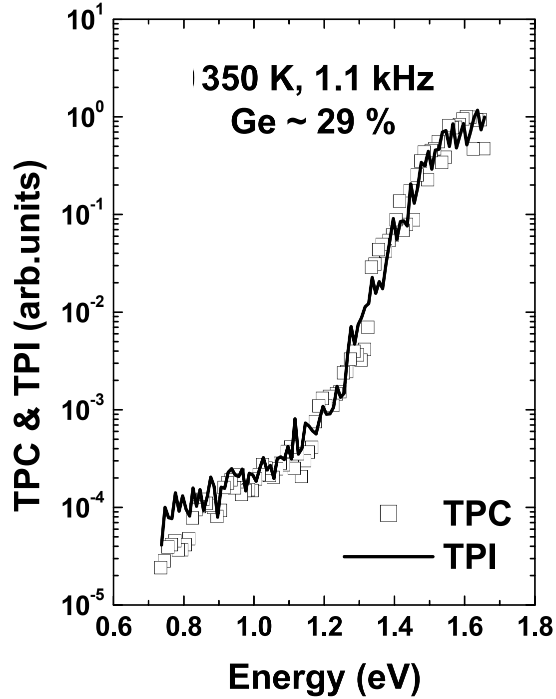

7.2 LIGHT-INDUCED DEGRADATION IN HWCVD a-Si,Ge:H

Finally, we have begun examining light-induced degradation in these HWCVD samples beginning with the 29at.% Ge sample. In Fig. 32 we display DLCP profiles of the midgap defect density as a function of exposure to tungsten-halogen light source filtered with a 610nm long pass filter. The net intensity was roughly 800 mW/cm^2, after correction for absorption in Pd top contact, and we were careful to keep the sample temperature below 330K. From the DLCP data in Fig. 32(a) we then estimated the spatial average of the relatively flat portion of these DLCP profiles to obtain the characteristic defect density at each *accumulated* light soaking time. This is displayed in Figure 32(b) and indicates two distinct steps in the defect creation process.

The unusual two-step time evolution of mid gap density exhibited for this sample with increasing light exposure is relatively unique to our knowledge. The increase in the defect density *following* the plateau after 4.5 hours of light soaking closely matches the familiar $t^{1/3}$ time dependence [10]. It is somewhat tempting to interpret the two stage increase seen in this sample along the lines of previous work on low Ge fraction (<20%) alloys in which it was reported [11] that there is an increase in the germanium dangling bonds, D^0_{Ge}, during the initial stages of light exposure followed by an ultimately larger increase of D^0_{Si} defects during the later stages of light soaking. On the other hand, it seems surprising that metastable D^0_{Si} defects should dominate the defect density in a a-Si,Ge:H alloy with Ge fraction as high as 29%.

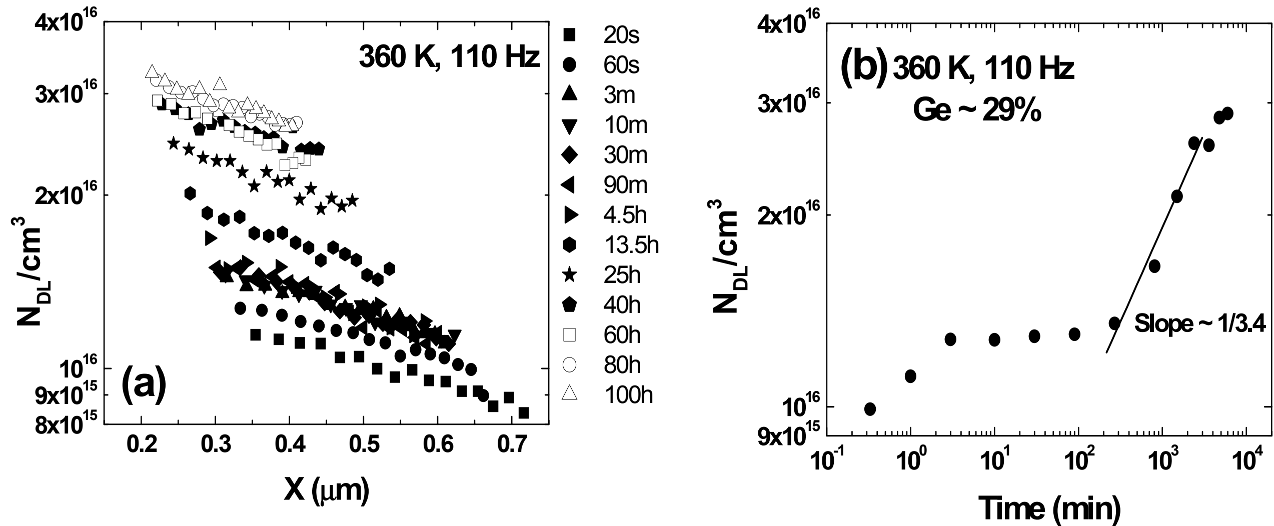

FIG. 32. (a) Spatial profile of mid gap densities as measured by DLCP method after increasing periods of light exposure for the 29at.% Ge sample. **(b)** Time dependence of the average midgap density with increasing light soaking indicates a two step process.

Further studies of the degradation kinetics of these alloys will be needed to establish the identity of the light induced defects responsible for the two-step behavior.

In Figure 33 we display the TPC spectra of 29at.% Ge sample at three stages of light soaking. These spectra have been aligned in the optical energy regime above 1.5 eV. It is clear that the defect band in the sub-band-gap spectral region also increases in a manner consistent with the results from the DLCP measurements.

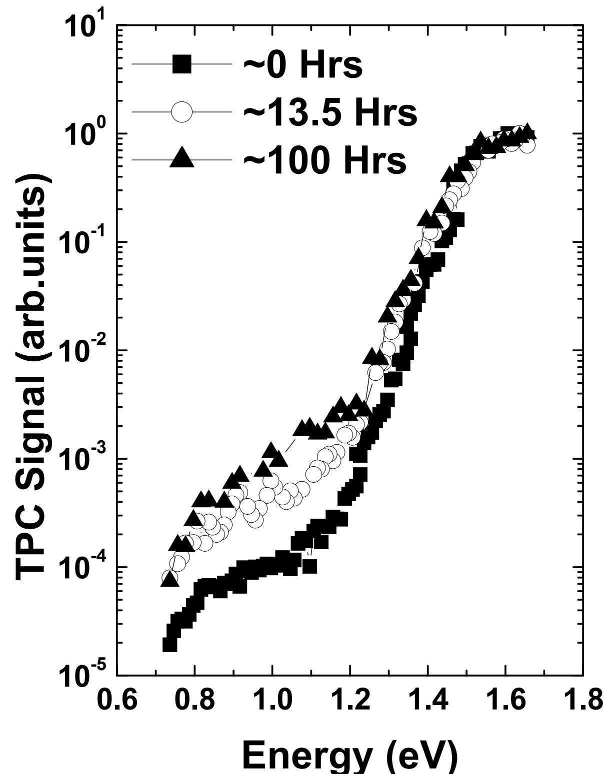

FIG. 33. Comparsion of the mid band-gap defect band for three photocapacitance spectra of the 29at.% Ge sample: In its pre-light-soaked state, after 13.5 hours exposure and after 100 hours of light exposure. The measurement temperature and frequency were 350K, 1.1 kHz before light soaking and 360 K, 1.1 kHz during light soaking. The changes in the magnitude of the deep defect feature agree quite well with those displayed in the DLCP spectra in Fig. 32.

8.0 ELECTRONIC PROPERTIES OF ECR DEPOSITED AMORPHOUS GERMANIUM

We characterized one sample device incorporating a-Ge:H deposited at Iowa State University using the ECR method. We employed the DLCP technique, and transient photocapacitance (TPC) spectroscopy, as described in Section 3 above. A series of 330Hz drive-level profiles is shown in Fig. 34 and indicates defect densities near the mid 10^{16} cm^{-3} level. The fact that these profiles do not change appreciably with temperature indicates that these defects must lie fairly close to the conduction band mobility edge. Specifically, to respond at 180K to the 330Hz oscillating voltage indicates an activation of less than 0.4eV.

In Fig. 35 we display both a transient photocapacitance and a junction transient photocurrent spectrum for this a-Ge:H sample. Both spectra are nearly identical and indicate a 42 meV Urbach energy and a defect band shoulder consistent with the DLCP estimate of a mid 10^{16} cm^{-3} defect density for this sample. These spectra also indicate an optical (E_{04}) optical gap of roughly 1.3eV. Such a narrow bandtail and low defect density indicate that this a-Ge:H material is of the highest quality. Indeed, it appears superior to all such samples we have measured with the possible exception of the Harvard cathodic glow discharge a-Ge:H samples.[35] In addition, the indicated high quality of these electronic properties is reflected in the excellent performance of the solar cell devices that has been demonstrated by the Dalal group for these alloy materials [7].

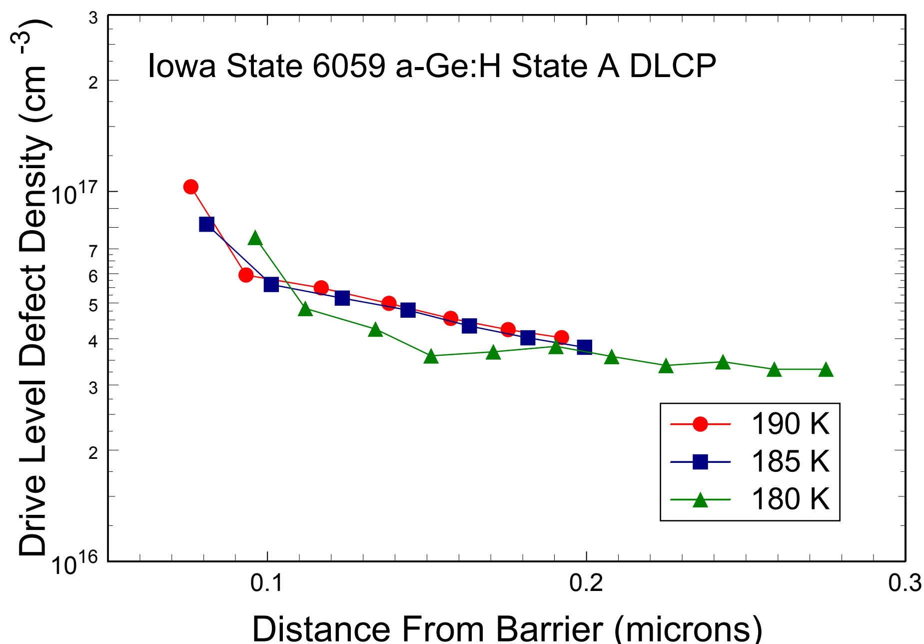

FIG. 34. Drive-level capacitance profiles of Iowa State ECR deposited a-Ge:H taken at 330Hz at three measurement temperatures. The defect density indicated is roughly 3.5 x 10^{15} cm^{-3} near the substrate of this a-Ge:H sample. The profiles are nearly temperature independent which indicates that the responding defects must be quite shallow (within 0.4eV of the conduction band mobility edge).

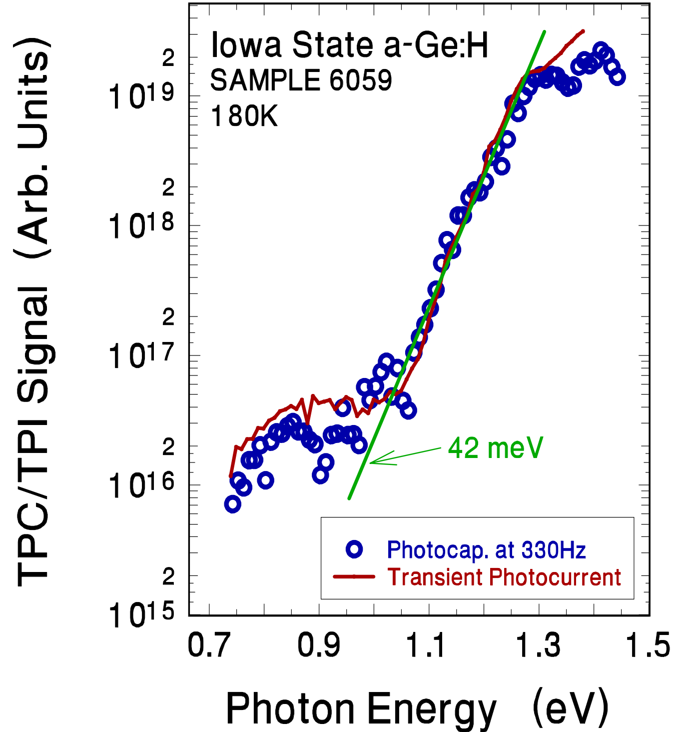

FIG. 35. Transient photo-capacitance and transient junction photocurrent spectra for Iowa State a-Ge:H sample 6059. Both spectra indicate an Urbach energy of 42meV, an E_{04} optical gap near 1.3eV, and a deep defect band consistent with the mid 10^{16} cm^{-3} level. This agrees with the DLCP measurements exhibited in Fig. 34.

9.0 SUMMARY AND CONCLUSIONS

One primary focus of our effort funded by NREL Subcontract ADJ-2-30630-17 period has been the characterization of hydrogenated nanocrystalline Si (nc-Si:H) produced at United Solar Ovonics Corporation. We applied both drive-level capacitance profiling (DLCP) and transient photocapacitance (TPC) spectroscopy for this purpose, and both methods were able to provide striking new insights into the electronic properties of this material. The DLCP studies of the nc-Si:H gave responding state densities in the 10^{15} to 10^{16} cm^{-3} range with very little temperature dependence. This indicates that the majority of these are relatively shallow states, within about 0.55eV of the conduction band. For 3 of the samples studied (two sandwich samples with capping a-Si:H layers as well as one purely nc-Si:H p-i-n device) we observed that the DLCP densities increased in the direction of film growth. This is consistent with observations at USOC that the crystallinity size increases as the films become thicker, and also suggests that there is an increasing density of deep defects with the increasing crystallite size. Moreover, the DLCP profiles on one nc-Si:H sample with intentional hydrogen profiling during growth (to maintain a more constant crystallite size) indicated a very different spatial profile, exhibiting a maximum near the middle of the nc-Si:H i-layer, plus a somewhat lower density than the corresponding samples deposited under constant hydrogen dilution.

Even more informative were our TPC spectroscopic measurements of these nc-Si:H samples. Here, and initially to great our surprise, we found that the TPC sub-band-gap evolved

from an appearance that agreed quite well at lower temperatures (200K) with previous sub-band-gap spectroscopic studies on μc-Si:H using methods such as CPM, but became very a-Si:H like in appearance at moderate temperatures (300K). By comparing the photocapacitance spectra with transient photocurrent spectra taken under the same conditions, this change in appearance of the TPC spectra with temperature was shown to be a result of improving hole carrier collection as the temperature was increased. That is, the higher the hole collection, the smaller the photocapacitance response of the nanocrystallite component compared to the amorphous silicon component since, for the latter, the hole carrier collection remains relatively poor even as the temperature is increased. These results were subsequently found to agree with x-ray diffraction measurements taken by Don Williamson on the USOC nc-Si:H material [20]. In addition, by examining the temperature dependence of the TPC spectra in detail, we determined that the hole collection was thermally activated, with an activation energy near 0.2eV. This suggests a dominant hole trap that impedes the minority carrier collection from the nanocrystallite phase of these nc-Si:H samples.

We also examined the effects of light-induced degradation in some detail for one of the nc-Si:H samples. The DLCP measurements actually showed very little change with light soaking, even after 100 hours at 100mW/cm^2. However, significant degradation in the hole carrier collection were observed in the TPC measurements, by nearly a factor of 50 at most temperatures. The activation energy for this hole collection did not change appreciably from that exhibited in the annealed state, however. This suggests, perhaps, that the type of hole trap is the same for both states A and B but that there are more of them after degradation. Finally, we did not observe any increase in any spectral feature, including the dangling bond defect band, that might be responsible for the observed loss in hole collection.

A second major focus during this Subcontract has been to continue our previous studies to identify the fundamental reasons that higher growth rate a-Si:H materials lead to devices with general lower performance. These studies utilized series of samples produced by Gautam Ganguly while still at BP Solar. During our previous Subcontract our measurements had revealed that the deep defect density determined by drive-level capacitance profiling (DLCP) did not change as the growth rate was varied; however, the Urbach energies deduced by transient photocapacitance (TPC) sub-band-gap spectroscopy *were* correlated with growth rate and hence also the device performance. During the first year of our new Subcontract we determined that the magnitude of the deep defect revealed in the TPC spectra actually correlated quite well with the device fill factors, even though the DLCP determined defect densities did not. This led us to propose that the capture cross section of the deep defects were enhanced at the higher growth rates even though their actual density did not vary substantially.

This led into a second study in collaboration with BP Solar employing a new series of their samples. Our own measurements were actually only one part of a 5-way collaboration designed to obtain one the most complete set of data ever undertaken to compare device and material properties as a function of deposition rate. Results for this new series of samples agreed with the previous set in that the DLCP determined defect densities appeared to be largely uncorrelated with device performance, while the Urbach energies were strongly correlated. The other collaborative studies revealed that the void fraction and the hydrogen content were also quite strongly correlated with growth rate. (The cell performance once again exhibited a systematic decline in performance with increasing growth rate.) At this point in time we can hypothesize that either the increased band-tail width (leading to a decreased effective hole mobility) or possibly the increase of deep defects with larger capture cross sections might be responsible. Either of these could be linked to the increased void fraction or changes in hydrogen microstructure.

The third area of focus has been to evaluate a new class of hot-wire deposited a-Si,Ge:H alloy samples produced at NREL. These were deposited using a Ta filament operated at 1800°C instead of a tungsten filament at 2000°C that had been used in the past. The HWCVD holds considerable promise since it is well known that deposition rates can be increased substantially for a-Si:H without detriment to the electronic properties. On the other hand, this had not been found to be true for the a-Si,Ge:H alloys since, even for modest Ge fractions of 20at.%, Urbach energies had been found to exceed 55meV and with correspondingly large defect densities. However, analysis using SAXS had shown that the low filament temperature a-Si,Ge:H material possessed a very low degree of structural disorder.

Photocapacitance and DLCP measurements on three of these HWCVD a-Si,Ge:H alloys with Ge fractions of 15, 29, and 47at.% did indeed disclose much improved electronic properties in terms of sharp band tails and midgap defect densities as low as the best PECVD grown alloy samples. These results thus directly corroborate the SAXS data indicating very uniform film structure with fewer micro-structural defects compared to previous a-Si,Ge:H alloys. However, when we compared the photocapacitance spectra with the corresponding transient photocurrent spectra, this indicated that minority hole collection was less efficient than the best PECVD grown alloy materials. This is puzzling given the very narrow bandtails, and further measurements are planned to better understand this result. Some preliminary light induced degradation studies on one (29at.% Ge) sample were also carried out. These revealed a novel two step defect creation process. These studies are continuing to try to identify the defects involved.

We wish also to briefly mention the results we obtained by examining a couple of amorphous germanium (a-Ge:H) samples produced by the ECR method at Iowa State University. Our studies indicated that these samples have quite superior electronic properties, both in terms of the DLCP deduced defect densities, and the TPC deduced Urbach energies. We thus believe that the ECR growth method may be the most suitable for producing high quality a-Si,Ge:H alloys in the high Ge fraction regime.

10.0 SUBCONTRACT SUPPORTED PUBLICATIONS

1. J. David Cohen, Jennifer Heath, Kimon C. Palinginis, Jeffrey C. Yang, and Subhendu Guha, “Insights into the mechanisms of light-induced degradation from studies of defects in low Ge fraction a-Si,Ge:H alloys”, J. Non-Cryst. Solids **299-302**, 449 (2002).

2. B. D. Chapman, S. -W. Han, G. T. Seidler, E. A. Stern, J. David Cohen, S. Guha and J. Yang, “Short-range compositional randomness of hydrogenated amorphous silicon-germanium films”, J. of Appl. Phys. **92**, 801 (2002).

3. Jennifer Heath, James J. Gutierrez, J. David Cohen, and Gautam Ganguly, “Effect of increasing growth rates on film properties and device performance for the DC glow discharge amorphous silicon”, Mat. Res. Soc. Symp. Proc. **715**, 553 (2002).

4. J. David Cohen, “Light-induced defects in hydrogenated amorphous silicon germanium alloys”, Sol. Energy Mat. and Solar Cells **78**, 399 (2003)

5. J. David Cohen, “Metastable defects in the amorphous silicon-germanium alloys”, Mat. Res. Soc. Symp. Proc. **762**, 51 (2003).

6. Jianhua Zhu, V.L. Dalal, M.A. Ring, J.J. Gutierrez, and J.D. Cohen, “Growth and properties of amorphous a-Ge:H solar cells”, J. Non-Crystalline Solids, **338-340**, 651-654 (2004).

7. J.J. Gutierrez, A.F. Halverson, E.D. Tweeten, J.D. Cohen, B. Yan, J.C. Yang, and S. Guha, “Electronic properties of RF glow discharge intrinsic microcrystalline silicon near the amorphous silicon phase boundary”, Mat. Res. Soc. Symp. Proc. **808**, 115 (2004).

8. Shouvik Datta, J. David Cohen, Yueqin Xu, and A. H. Mahan, “Electronic properties of improved amorphous silicon-germanium alloys deposited by a low temperature hot-wire chemical vapor deposition process”, Mat. Res. Soc. Symp. Proc. **862** , in press.

9. Adam F. Halverson, James .J. Gutierrez, J.David Cohen, Baojie Yan, Jeffrey Yang, and Subhendu Guha, “The Effects of Hydrogen Profiling and of Light-Induced Degradation on the Electronic Properties of Hydrogenated Nanocrystalline Silicon”, Mat. Res. Soc. Symp. Proc. **862** , in press.

10. Baojie Yan, Jeffrey Yang, Subhendu Guha, D.L. Williamson, Daxing Han, Keda Wang, Adam F. Halverson, James J. Gutierrez, and J. David Cohen, “Evidence of controlling nanocrystalline structure evolution in hydrogrenated nanocrystalline silicon deposition using hydrogen dilution profiling technique”, submitted to Applied Physics Letters.

11.0 REFERENCES

1. B. Yan, G. Yue, J. Yang, S. Guha, D. L. Williamson, D. Han, and C.-S. Jiang, Appl. Phys. Lett. 85, 1955 (2004).
2. J. Yang, K. Lord, B. Yan, A. Banerjee, and S. Guha, Mat. Res. Soc. Symp. Proc. **715**, 601 (2002).
3. J. D. Cohen, Final Subcontract Report 16 January 1998-15 October 2001, NREL Technical Publication No.: NREL/SR-520-32535.
4. J. Heath, S.B. Iyer, Y. Lubianiker, J.D. Cohen, and G. Ganguly, Mat. Res. Soc. Symp. Proc. **664**, A25.3 (2001)
5. D.L. Williamson, G. Goerigk, Y. Xu, and A.H. Mahan, Proceedings DOE Solar Energy Technologies Review Meeting, DOE/GO-102005-2067 (2005) p. 444.
6. Y. Xu, B. P. Nelson, D. L. Willamson, L. M. Gedvilas, R.C. Reddy, Mat. Res. Soc. Symp. Proc. **762**, A10.2 (2003).
7. Yong Liu and Vikram L. Dalal, Mat. Res. Soc. Symp. Proc. **715**, 515 (2002).
8. D.V. Lang, J.D.Cohen, and J.P. Harbison, Phys. Rev. B**25**, 5285 (1982).
9. C.E. Michelson, A.V. Gelatos, and J.D. Cohen, Appl. Phys. Lett. **47**, 412 (1985).
10. K.K. Mahavadi, K. Zellama, J.D. Cohen, and J.P. Harbison, Phys. Rev. B**35**, 7776 (1987).
11. J.D. Cohen and A.V. Gelatos, in *Advances in Disordered Semiconductors Vol I: Amorphous Silicon and Related Materials*, ed. by H. Fritzsche (World Scientific, Singapore, 1988), pp. 475-512.
12. J. David Cohen, Thomas Unold, A.V. Gelatos, and C.M. Fortmann, J. Non-Cryst. Solids **141**, 142 (1992).
13. T. Unold, J.D. Cohen, and C.M. Fortmann, Mat. Res. Soc. Symp. Proc. **258**, 499 (1992).
14. A.V. Gelatos, K.K. Mahavadi, and J.D. Cohen, Appl. Phys. Lett. **53**, 403 (1988).
15. Chih-Chiang Chen, Fan Zhong, J.D. Cohen, Jeffrey C. Yang, and Subhendu Guha, Phys. Rev. B**57**, R4210 (1998).
16. D. Kwon, C.-C. Chen, and J.D. Cohen, H.-C. Jin, E. Hollar, I. Robertson, and J.R. Abelson, Phys. Rev. B**60**, 4442 (1999).
17. J. Meier, R. Flückiger, H. Keppner, and A. Shah, J. Appl. Phys., **65**, 860 (1994).
18. See, for example, Y. Tawada, H. Yamagishi and K. Yamamoto, Sol. Energy Mat. and Sol. Cells, 78, 647 (2003).
19. P. Torres, J Meier, R. Flückiger, U. Kroll, J. A. Anna Selvan, H. Keppner, and A. Shah, J. Appl. Phys., **69**, 2286 (1996)
20. B. Yan, G. Yue, J. Yang, S. Guha, D. L. Williamson, D. Han and C.S. Jiang, Mat. Res. Soc. Symp. Proc. **808**, 575 (2004).

21. See, for example, H-R. Park, D. Kwon, and J.D. Cohen, J. Appl. Phys. **83**, 8051 (1998).
22. M. Vaněček and A. Poruba, Appl. Phys. Lett. **80**, 719 (2002).
23. Baojie Yan, private communication.
24. A.V. Shah, J. Meier, E. Vallat-Sauvain, N. Wyrsch, U. Kroll, C. Droz, U. Graf, Sol. Energy Mat. Sol. Cells, **78**, 469 (2003).
25. P. Torres, J Meier, R. Flückiger, U. Kroll, J. A. Anna Selvan, H. Keppner, and A. Shah, J. Appl. Phys., **69**, 2286 (1996).
26. B. Yan, G. Yue, J. M. Owens, J. Yang, and S. Guha, Appl. Phys. Lett. 85, 1925 (2004).
27. See, for example, T. Unold, J. Hautala, and J.D. Cohen, Phys. Rev. B**50**, 16985 (1994).
28. X. Xu, J. Yang, S.and S. Guha, Appl. Phys. Lett. **62**, 1399 (1993).
29. B. von Roedern, Appl. Phys. Lett. **62**, 1368 (1993).
30. C.R. Wronski, J.M. Pearce, R.J. Koval, X. Niu, A.S. Ferlauto, J. Koh, and R.W. Collins, Mat. Res. Soc. Symp. Proc. **715**, 459 (2002).
31. See, for example, M. Gunes and C.R. Wronski, J. Appl. Phys. **81**, 3526 (1997).
32. A.H. Mahan, R.C. Reedy Jr., E. Iwaniczko, Q. Wang, B.P. Nelson, Y. Xu, A.C. Gallagher, H.M. Branz, R.S. Crandall, J. Yang, and S. Guha, MRS Symp. Proc. No. **507** (Materials Research Society, Pittsburgh,1998), p. 119.
33. D.L. Williamson, G. Goerigk, Y. Xu, and A.H. Mahan, Proceedings DOE SolarEnergy Technologies Review Meeting, DOE/GO-102005-2067 (2005) p. 444.
34. Y. Xu, B. P. Nelson, D. L. Willamson, L. M. Gedvilas, R.C. Reddy, Mat. Res. Soc. Symp. Proc. 762, A10.2 (2003).
35. Paul Wickboldt, Dawen Pang, William Paul, Joseph H. Chen, Fan Zhong, Chih-Chiang Chen, J.David Cohen, and Don L. Williamson, J. Appl. Phys. **81**, 6252 (1997).

REPORT DOCUMENTATION PAGE	*Form Approved* *OMB No. 0704-0188*

The public reporting burden for this collection of information is estimated to average 1 hour per response, including the time for reviewing instructions, searching existing data sources, gathering and maintaining the data needed, and completing and reviewing the collection of information. Send comments regarding this burden estimate or any other aspect of this collection of information, including suggestions for reducing the burden, to Department of Defense, Executive Services and Communications Directorate (0704-0188). Respondents should be aware that notwithstanding any other provision of law, no person shall be subject to any penalty for failing to comply with a collection of information if it does not display a currently valid OMB control number.

PLEASE DO NOT RETURN YOUR FORM TO THE ABOVE ORGANIZATION.

1. **REPORT DATE** *(DD-MM-YYYY)*	2. **REPORT TYPE**	3. **DATES COVERED** *(From - To)*
November 2005	Subcontract Report	27 November 2002–31 March 2005

4. TITLE AND SUBTITLE
Identifying Electronic Properties Relevant to Improving the Performance and Stability of Amorphous Silicon Based Photovoltaic Cells: Final Subcontract Report, 27 November 2002–31 March 2005

5a. CONTRACT NUMBER
DE-AC36-99-GO10337

5b. GRANT NUMBER

5c. PROGRAM ELEMENT NUMBER

6. AUTHOR(S)
J.D. Cohen

5d. PROJECT NUMBER
NREL/SR-520-38676

5e. TASK NUMBER
PVB65101

5f. WORK UNIT NUMBER

7. PERFORMING ORGANIZATION NAME(S) AND ADDRESS(ES)
Dept. of Physics and Materials Science Institute
University of Oregon
Eugene, Oregon

8. PERFORMING ORGANIZATION REPORT NUMBER
ADJ-2-30630-17

9. SPONSORING/MONITORING AGENCY NAME(S) AND ADDRESS(ES)
National Renewable Energy Laboratory
1617 Cole Blvd.
Golden, CO 80401-3393

10. SPONSOR/MONITOR'S ACRONYM(S)
NREL

11. SPONSORING/MONITORING AGENCY REPORT NUMBER
NREL/SR-520-38676

12. DISTRIBUTION AVAILABILITY STATEMENT
National Technical Information Service
U.S. Department of Commerce
5285 Port Royal Road
Springfield, VA 22161

13. SUPPLEMENTARY NOTES
NREL Technical Monitor: Bolko von Roedern

14. ABSTRACT *(Maximum **200 Words**)*
A major effort during this subcontract period has been to evaluate the microcrystalline Si material under development at United Solar Ovonics Corporation (USOC). This material is actually a hydrogenated nanocrystalline form of Si and it will be denoted in this report as nc-Si:H. Second, we continued our studies of the BP Solar high-growth samples. Third, we evaluated amorphous silicon-germanium alloys produced by the hot-wire chemical vapor deposition growth process. This method holds some potential for higher deposition rate Ge alloy materials with good electronic properties. In addition to these three major focus areas, we examined a couple of amorphous germanium (a-Ge:H) samples produced by the ECR method at Iowa State University. Our studies of the electron cyclotron resonance a-Ge:H indicated that the Iowa State a-Ge:H material had quite superior electronic properties, both in terms of the drive-level capacitance profiling deduced defect densities, and the transient photocapacitance deduced Urbach energies. Also, we characterized several United Solar a-Si:H samples deposited very close to the microcrystalline phase transition. These samples exhibited good electronic properties, with midgap defect densities slightly less than 1×10^{16} cm^{-3} in the fully light-degraded state.

15. SUBJECT TERMS
PV; module; solar cell; thin film; amorphous silicon; drive-level capacitance profiling (DLCP); modulated photocurrent spectroscopy (MPS); electronic properties; electron cyclotron resonance (ECR); hot-wire chemical vapor deposition; transient photocapacitance (TPC)

`+			17. LIMITATION OF ABSTRACT	18. NUMBER OF PAGES	19a. NAME OF RESPONSIBLE PERSON
a. REPORT	b. ABSTRACT	c. THIS PAGE			
Unclassified	Unclassified	Unclassified	UL		19b. TELEPONE NUMBER *(Include area code)*

Standard Form 298 (Rev. 8/98)
Prescribed by ANSI Std. Z39.18

F1146-E(05/2004)